ELECTRIC FIELD-ENHANCED DIFFUSION AND ELECTRON STIMULATED DESORPTION OF ALKALI ELEMENTS FROM GLASS SURFACES DURING ELECTRON BOMBARDMENT AND AUGER ELECTRON ANALYSIS

BY

FUMIO OHUCHI

A DISSERTATION PRESENTED TO THE GRADUATE COUNCIL OF
THE UNIVERISTY OF FLORIDA
IN PARTIAL FULFILLMENT OF THE REQUIREMENTS FOR THE
DEGREE OF DOCTOR OF PHILOSOPHY

UNIVERSITY OF FLORIDA

1981

To

My Wife Sumiyo and My Mother Teiko

Bound by DOBBS BROS. LIBRARY BINDING CO., INC.,

ACKNOWLEDGEMENT

The author would like to acknowledge and thank his advisory committee and, in particular, to express his gratitude to Professors P. H. Holloway and L. L. Hench, who convinced the author of the importance of his research and maintained an open and creative research environment throughout the course of this work. Also, the author would like to acknowledge Professor C. G. Pantano, Jr.,of The Pennsylvania State University, who introduced him to these dissertation topics and offered invaluable encouragement and advice.

In addition, thanks are extended to M. Ogino, Nippon Kogaku K. K., for his helpful discussions. The technical assistance of S. K. Hofmeister is also appreciated.

With deepest gratitude, the author wishes to acknowledge his wife, Sumiyo, for her constant encouragement and inspiration. Also, he wishes to thank his mother for her lifelong encouragement and support.

Finally, the financial support of the Air Force Office of Scientific Research (Grant No. 77-3210) was appreciated.

TABLE OF CONTENTS

PAGE

ACKNOWLEDGEMENT....................iii

LIST OF TABLES....................vi

LIST OF FIGURES....................vii

ABSTRACT....................xi

CHAPTER

I INTRODUCTION....................1

Overview....................1
Background and Qualitative Assessment....................3
    Interaction of Electrons with Glass....................3
    Electron Beam Effects....................4
    Compositional Change in Auger Electron Spectroscopy....................5
    Electron Beam Induced Alkali Diffusion....................8
    Electron Beam Induced Alkali Volatilization and Desorption....................15
Research Plan....................18

II DIFFUSION OF SODIUM DURING ELECTRON BOMBARDMENT....................21

Experimental Procedure....................21
Results....................23
A Model for Field-Enhanced Diffusion....................31
Discussion....................36
    A Model Calculation and Estimation of Field Strength....................36
    Sodium Depth Profile....................40
Summary....................44

III DESORPTION OF SODIUM DURING ELECTRON BOMBARDMENT....................46

Experimental Procedure....................46
Results....................48
Phenomenological Model of ESD on Glass Surface....................59
    A Model....................59
    Mathematical Formulation of Model....................60
    Solution....................63
    Model Calculation....................65
Mechanism for Sodium Desorption from Glass....................68
Discussion....................75
Summary....................81

CHAPTER PAGE

IV THEORETICAL INTERPRETATION OF ALKALI AUGER SIGNAL DECAY......83

Mathematical Formulation of Alkali Auger Signal Intensity....84
Discussion...89
    A Model Calculation..89
    Comparison of Experimental Results with Model..............94
Summary..99

V APPLICATION OF ALKALI AUGER SIGNAL DECAY PROCESS FOR MATERIAL CHARACTERIZATION..................................101

Experimental Procedure..102
Results...104
Discussion..111
Summary...114

VI SUMMARY AND CONCLUSIONS....................................116

APPENDICES

A SOLUTION OF EQUATION (3)......................................120

B SOLUTION OF EQUATION (12).....................................124

C CONVOLUTION THEOREM...126

D ELECTRON BEAM HEATING...127

BIBLIOGRAPHY..128

BIBLIOGRAPHICAL SKETCH..138

LIST OF TABLES

TABLE		PAGE
1	Summary of Calculated Results for the Conversion and the Electron Stimulated Desorption Cross Sections	69
2	Critical Electron Dose for Electron Bombardment Damage of Molecular Solids and Films (from [123])	98
3	Specimen Preparation Data	103

LIST OF FIGURES

FIGURE		PAGE
1	Comparison of AES spectra for (a) a freshly created surface and (b) a surface with extensive electron irradiation prior to the measurement of soda-disilicate glasses, and (c) a fused silica. A 3 keV, 5 mA/cm^2 electron beam was used.	6
2	Comparison of IRRS spectra for soda-disilicate glass surface before (curve (1)) and after (curve (2)) electron bombardment, and a fused silica surface. A 25 keV electron beam was used for bombardment in a scanning electron microscope (JEOL-35c).	7
3	Variation of the secondary electron emission yield as a function of the primary beam energy.	10
4	Schematic representation of the electric field produced normal to the surface as a result of the surface positive potential and the diffused negative layer at a depth equal to the electron range.	12
5	Normalized Auger sodium signal decay from a soda-lime-silica glass at both room temperature and liquid nitrogen temperature using a beam diameter of 500 μm at 3 keV for various levels of beam current (from [39]).	14
6	a) Optical microscope photograph of a soda-lime-silica glass membrane showing a hole by melting as a result of electron beam heating. b) A photograph showing collapsed soda-lime-silica glass fiber as a result of electron beam heating. A 3 keV, 100 mA/cm^2 electron beam was used.	16
7	AES spectrum from a 1000 Å thick glass film deposited on a stainless steel substrate, taken using a 3 keV electron beam with a total current of 5 μA at liquid nitrogen temperature (110° K).	24
8	Sodium Auger peak height as a function of beam impingement time and glass thickness for a 3 keV electron beam with a current density of 5 mA/cm^2 at room temperature.	26

PAGE

9 Sodium Auger peak height as a function of beam impingement time from a 2000 Å thick film for energies ranging from 1.5 to 10 keV. The beam current density was 1.4 mA/cm^2 and the analysis was performed at room temperature (300° K). 27

10 Sodium Auger peak height as a function of beam impingement time from a 2000 Å thick film at room temperature. A 3 keV electron beam was used with the current densities varied between 1.4 mA/cm^2 and 1.25 A/cm^2. 29

11 Sodium Auger peak height as a function of beam impingement time from a 1000 Å thick film for a 3 keV electron beam with current density of 5 mA/cm^2 at liquid nitrogen (110° K) and room temperature (300° K). 30

12 Schematic illustration of the electron beam penetration and the charge accumulation in glass film for low and high energy electrons. 33

13 Schematic illustration of the model used to calculate sodium ion diffusion. 34

14 Calculated sodium decay curves (solid lines) that are best fit to the experimental data shown in Figure 8. 38

15 Calculated sodium distribution in the film after electron beam impingement for time t, when $t_1 = 0 < t_2 < t_3 < t_4 < t_5$. 41

16 Sodium concentration depth profile in the 1000 Å glass film from an unirradiated area (shown by dotted curve) and an irradiated area (shown by solid curve). Iron signal profile is shown by broken line curve. 42

17 Experimental configuration for threshold energy measurement of ESD. 49

18 ESD spectra from a soda-silica glass surface exposed to a pressure of 1×10^{-9} Torr for 10 minutes. (a) For 90 minutes, (b) after an *in situ* fracture. A 1 keV, 1 mA/cm^2 electron beam was used. 50

19 A desorption rate profile of m/e = 16 and 23 signals from the soda-silica glass surface as a function of electron beam bombardment time. A 1 keV, 1 mA/cm^2 electron beam was used. 52

PAGE

20 A desorption rate profile of m/e = 23 (Na^+) signal from the soda-silica glass surface as a function of electron dose. Figures (a), (b), (c) and (d) are for the energies of 0.5, 1, 2 and 4 keV, respectively, with varying beam current densities shown in figures. 54, 55

21 A plot of maximum desorption rates of sodium from the soda-silica glass surface as a function of beam current density at 2 keV. 56

22 A desorption rate profile of m/e = 16 (O^+) signals from the soda-silica glass surface as a function of electron dose at 2 keV. 57

23 A plot of oxygen (KLL) Auger peak height from the soda-silica glass surface as a function of electron dose at 2 keV. 58

24 Calculated desorption rates of sodium from the soda-silica glass surface that are best fit to the experimental data reproduced from Figure 20. 67

25 Interatomic Auger de-excitation model for stimulated desorption of ions. Formulation of a core hole in the 3p shell of maximal valency TiO_2 is followed by interatomic Auger decay. 71

26 Interatomic Auger de-excitation model for stimulated desorption of sodium ions. After a hole trapping in non-bridging oxygen 2p orbital of a single oxygen, formulation of a core hole in the 2p shell of maximal valency of Si is followed by interatomic Auger decay. 72

27 Sodium desorption yield from a soda-silica glass surface versus electron energy. 74

28 Calculated maximum desorption rate of sodium from the soda-silica glass surface as a function of beam current density. 80

29 Calculated sodium Auger signal decay from soda-silica glass. 91

30 Schematical illustration of relations for $C_1(t)$, $C_2(t)$ and $n^A(t)$ at low temperature and room temperature. 93

31 Normalized sodium Auger peak height from soda-disilicate glass as a function of electron beam bombardment time at liquid nitrogen and room temperatures. A 3 keV, 1 mA/cm^2 electron beam was used. 95

PAGE

32 Normalized sodium Auger peak height from a soda-disilicate glass as a function of electron dose at liquid nitrogen temperature (110° K). 96

33 Scanning electron micrographs of etched fracture surface of lithia-disilicate glass containing: (a) more than 70% crystallization and (b) approximately 50% crystallization. 105

34 Lithium Auger peak height as a function of beam exposure time and beam current density for lithia-disilicate glass at liquid nitrogen temperature (110° K). 106

35 Lithium Auger peak height as a function of beam exposure time and beam current density for lithia-disilicate glass containing 30% crystallization at liquid nitrogen temperature. 108

36 Lithium Auger peak height as a function of beam exposure time for various volume fractions of crystallization. 109

37 Lithium Auger peak height as a function of substrate temperature for 33L glass containing 30% crystallization. 110

Abstract of Dissertation Presented to the Graduate Council
of the University of Florida in Partial Fulfillment of the
Requirements for the Degree of Doctor of Philosophy

ELECTRIC FIELD-ENHANCED DIFFUSION AND ELECTRON STIMULATED DESORPTION OF ALKALI ELEMENTS FROM GLASS SURFACES DURING ELECTRON BOMBARDMENT AND AUGER ELECTRON ANALYSIS

By

Fumio Ohuchi

March, 1981

Chairman: Paul H. Holloway
Major Department: Materials Science and Engineering

Among a number of modern surface sensitive analytical techniques, Auger electron spectroscopy (AES) has been extensively applied for glass surface research because of its superior characteristics. AES has been generally considered as a "non-destructive" technique; however, a number of reports have shown that the incident electron beam can alter the surface composition of the solid being analyzed. Compositional changes in glass have been particularly severe in glasses containing alkali ions and it has been manifested by the time-dependent alkali Auger signal loss during electron bombardment.

The present work describes fundamental mechanisms of alkali Auger signal loss from glass surfaces during electron bombardment. It has been shown that this is the result of electric field enhanced diffusion and electron stimulated desorption. Electric field enhanced diffusion was demonstrated in soda-silica glass thin films deposited on stainless steel substrates. The amount of charge trapping was controlled by the experimental conditions and the electric field strength in glass was evaluated to be approximately 10^5 V/cm. Electron stimulated desorption was studied from soda-silica glass fibers fractured *in situ*. It was found that sodium and oxygen were desorbed during electron bombardment. Electron stimulated desorption became important with beam current densities greater than 10^{-3} A/cm^2, and the field enhanced diffusion limited further increase in desorption of sodium with a current density greater than 5×10^{-2} A/cm^2. The desorption cross section for sodium was found to be about $10^{-19} cm^2$ for the primary electron energy of 0.5 to 4.0 keV. The desorption mechanism was also studied. A Menzel-Gomer-Redhead model was not adequate to explain sodium desorption from glass, but a core hole Auger decay model was the most likely mechanism. Thereby the cross section was correlated with this mechanism and reasonable agreement with experimental results was made.

A comprehensive theory for the alkali Auger signal loss has been developed. This was applied to low temperature measurements and the origin of the incubation time (during which the alkali Auger signal was nearly consistent) became apparent.

AES has been applied to the investigation of microstructural characterization of lithia-silica glass-ceramics. The rates of lithium Auger signal loss were influenced by the presence of a crystalline phase and were correlated with the volume percent of crystallization.

CHAPTER I
INTRODUCTION

Overview

The variation of glasses used in industrial and laboratory applications is extensive. For many uses treatments such as polishing, etching, chemical cleaning and heat treatment are performed to control properties related to reflectivity, hardness, chemical durability or adhesion. For these uses, knowledge of the chemical surface composition would help to make more reliable predictions of properties. Unfortunately, numerous surface phenomena and characteristics are not yet explained due to the difficulties of these measurements. Classical techniques can provide information about the outer few thousand Angströms of glass; however, these techniques are generally slow and have poor depth resolution.

In recent years modern surface sensitive analytical techniques, such as Auger Electron Spectroscopy (AES) [1], Electron Spectroscopy for Chemical Analysis (ESCA) [2], Secondary Ion Mass Spectroscopy (SIMS) [3], Ion Scattering Spectroscopy (ISS) [4], Sputter Induced Photon Spectroscopy (SIPS) [5] and Rutherford Backscattering Spectroscopy (RBS) [6] have been extensively developed. A common feature of these techniques is that the sample is brought into a vacuum chamber where it is bombarded with a beam of energetic particles such as electrons, ions or photons and the interaction of these beams with the sample produces secondary particles which can be analyzed to obtain information from a thin surface layer. All of these techniques except RBS are sensitive to the outermost atomic layers of a solid; therefore any change in the concentration or chemical state of surface species will be immediately evident.

The technique of Auger Electron Spectroscopy is used extensively for glass surface research because of its good spatial resolution, rapid data acquisition, relatively easy interpretation of data, capability for at least semiquantitative analysis, wide elemental detection range (all elements except H and He) and high sensitivity for low atomic number elements commonly used in glass constituents.

Auger Electron Spectroscopy is generally considered to be a "nondestructive" technique. However, there are many instances where the incident electron beam can alter the surface composition of the solid being analyzed [7-67]. Compositional changes in glass during electron irradiation for AES have been reported by several investigators [11,35, 36,39,44,45,48]. Changes are particularly severe in glasses containing alkali ions. An increase or decrease of intensity, a change in energy and/or a change in Auger peak shape may be associated with electron bombardment time. Such effects must be at least minimized in order to perform a meaningful analysis.

The purpose of this research is to obtain a better understanding of the effects of electron beam irradiation upon the surface of glasses. The topics are rather specific to the problem associated with sodium ion diffusion and desorption in glasses induced by electron irradiation for Auger electron analysis, but the conclusions will be shown to be generally applicable to other alkali ions.

Background and Qualitative Assessment

Interaction of Electrons With Glass

When a glass is exposed to an electron beam, numerous changes in the physical and chemical properties of the glass surface can take place. For example, the glass surface composition can be altered, an optical absorption band may be induced, the density of the glass surface can change, paramagnetic defect centers can be formed, microscopic phase separation can be induced and the physical and chemical strength of the glass surface can be altered [68,69]. These phenomena all result from the interaction between electrons and the glass surface and will be referred to collectively as "electron beam effects."

Electron beam effects are consequences of interaction of electrons with the glass. Impinging electrons with energies less than 20 keV are scattered elastically or inelastically [70] and can cause changes in the electronic state of atoms near the surface. The electrons move through the glass matrix and will either create a dangling bond in the glass structure [68,69], be trapped by pre-existing flaws to form defect centers in the glass structure [68], recombine with the positively-charged hole [68], or produce a secondary electron cascade by knock-on collisions with the bound electrons [68,69]. Secondary electrons, created by primary electrons through the matrix, ionize additional bound electrons by Coulombic interactions and lose energy for each ionization. Finally, the electrons will not have enough energy to ionize the atom, therefore they become trapped at defects or recombine with positive holes in the matrix. These electronic excitations result in damage near the surface.

Electron Beam Effects

Although the early interest in the radiation effect on glass originated from the observation by Roentgen that the glass door knob on the inside of his x-ray room turned blue, a realization that electron beams affect glass is relatively new. Such effects were first observed on glass envelopes, which limited the lifetimes of cathode ray tubes [49]. Todd and Lineweaver [50] found that the electron bombardment of glasses containing alkali elements led to oxygen outgassing and browning of the glass. These phenomena have usually been explained in terms of a mechanism proposed by Lineweaver [51]. According to his mechanism, the high energy electrons traverse a thickness equivalent to their range and come to rest, producing a net negative charge in the glass. This net electrical charge creates an electric field in the glass. Under the influence of this electric field, the positive alkali ions present in the glass diffuse away from the surface and the oxygen ions move toward the surface and are desorbed into the vacuum.

Several Electron Microprobe (EMP) studies on alkali-containing glasses [52-61] apparently supported the Lineweaver mechanism. The decay of the x-ray signal from the alkali atom could only mean that alkali atoms were leaving the volume in which the incident electrons had sufficient energy to excite x-ray emission. Although the creation of an internal electric field under electron bombardment is likely, no measurement has been reported on the magnitude of the electric field.

Compositional Change in Auger Electron Spectroscopy

In the 1970's, Auger Electron Spectroscopy (AES) became popular and was applied to glass surface analysis. Goldstein and Carlson [62] measured Auger spectra for an alkali-strontium-silica glass, while Rynd and Rastogi [63,64] used AES to characterize glass fiber surfaces. Chappell and Stoddart [35] used AES to investigate the effects of the float glass process upon the surface composition. Pantano, Clark and Hench [65] used AES to examine the sequence of chemical reactions at a soda-lime-silica glass surface during aqueous attack. A common observation in the above studies was the absence of alkali at the surface or the rapid decrease of alkali Auger signal in a fashion similar to the EMP study. However, the problem in the case of AES is much more severe, since the Auger escape depth is ~ 10 Å [66] in comparison to ~ 1 μm in the EMP [67]. Therefore, any change within a few atomic layers causes a noticeable variation in the Auger signal intensity.

Figure 1(a) and (b) compare the Auger spectra of a freshly created surface and a surface with extensive electron irradiation prior to Auger measurement of soda-disilicate glass. Obvious differences are seen in the intensity of the sodium Auger peaks. Comparing the spectrum in Figure 1(b) with an Auger spectra from fused silica shown in Figure 1(c), little difference is noticed in terms of peak height ratio of Si/O. This indicates that electron irradiation changes the surface composition of the soda-disilicate glass to a composition similar to fused silica.

This similarity is further substantiated by infrared reflection spectra, as shown in Figure 2. Curves (1), (2) and (3) are the spectra

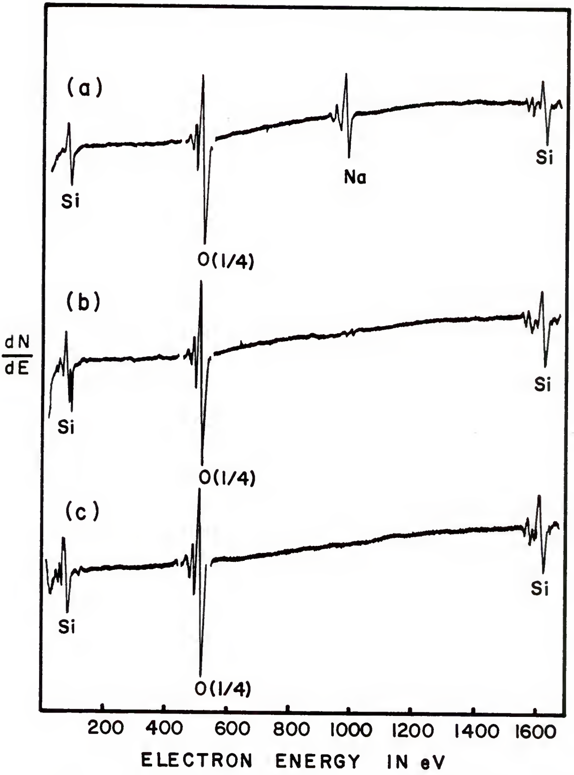

Figure 1. Comparison of AES spectra for (a) a freshly created surface and (b) a surface with extensive electron irradiation prior to the measurement of soda-disilicate glasses, and (c) a fused silica. A 3 keV, 5 mA/cm^2 electron beam was used.

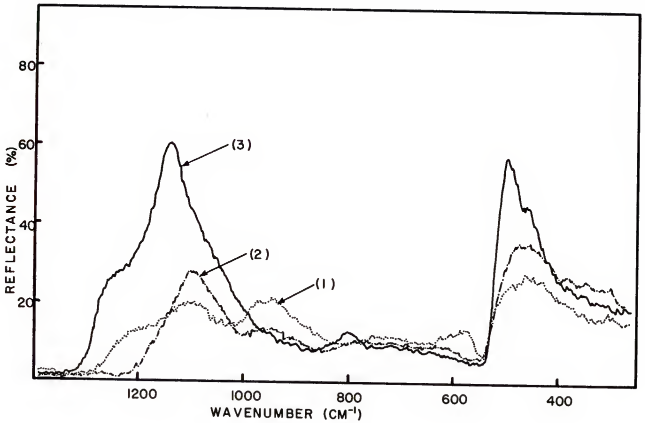

Figure 2. Comparison of IRRS spectra for soda-disilicate glass surface before (curve (1)) and after (curve (2)) electron bombardment, and a fused silica surface. A 25 keV electron beam was used for bombardment in a scanning electron microscope (JEOL-35c).

from the soda-disilicate glass surface before and after electron beam irradiation and from the fused silica, respectively. The spectrum for the electron irradiated surface shows a shift in the Si-O vibrational mode toward the value observed for the fused silica (1100 cm^{-1}) [71]. The Si-O vibrational mode in curve (2) also assumes an overall shape similar to that observed from fused silica. A NBO stretching peak at 960 cm^{-1} [71] observed in curve (2) is very weak as compared to curve (1). This indicates that the sodium is depleted at least within the infrared information depth (~ .5 μm [72]).

The alkali Auger signal loss can be caused by the disappearance of alkali at the surface due to either its diffusion into the bulk or its escape into the vacuum. Surface diffusion can also cause the compositional change, particularly in Auger microanalysis when an extremely small electron beam is used [73]. In a typical analysis of a glass surface, either an electron beam scanning a relatively large area or a de-focused electron beam can be used to reduce the electron beam current density. When this is done, surface diffusion can be ruled out because a measurable signal loss is greater than the radius of the electron beam. Since a measurable signal loss still occurs, both diffusion into the bulk and escape from the surface has to be studied more carefully in order to understand the beam effects.

Electron Beam Induced Alkali Diffusion

The surface of a glass is normally electrically isolated from ground but has an incident electron current entering and a secondary electron current leaving the sample. The electrical state of the surface is therefore largely governed by the ratio of outgoing to incoming current, i.e., by the secondary electron emission yield, δ. The dependence of the yield, δ, on primary beam energy, E_p, is shown in Figure 3 [70]. When the yield is less than unity, the surface is negatively charged due to the accumulation of negative charges on the surface. Under these conditions, meaningful Auger spectra are often difficult to obtain [74]. The surface potential may reach a high negative value close to the breakdown voltage and dielectric breakdown may occur [75] and disturb the Auger spectra. A positive surface potential develops when the yield is greater than unity. This occurs in the energy range between E_{p1} and E_{p2} where most AES data are collected. In this case, low energy secondary electrons can return to the surface and prevent excessive surface potentials. The higher δ is, the higher the positive charge should be. In the case of SiO_2, the maximum of δ is reached near 400 eV [76].

The influence of the angle of incidence of the electron beam on the surface charge is also critical. When this angle is increased, the yield increases and the positive surface charge is expected to increase. This is demonstrated by data from Jassen et al. [77] on MgO. The oxygen Auger peak shifted 10 eV lower in energy as the angle of incidence was increased from 0° to 80° with respect to the plane of the surface. The electron beam energy and angle of incidence are thus critical to prevent charging [78]. Upon development of a stable positive surface potential, the Auger spectrum can be obtained. However, the positive surface potential shifts the Auger peaks anywhere from 2 to 10 eV lower in energy. In this case,

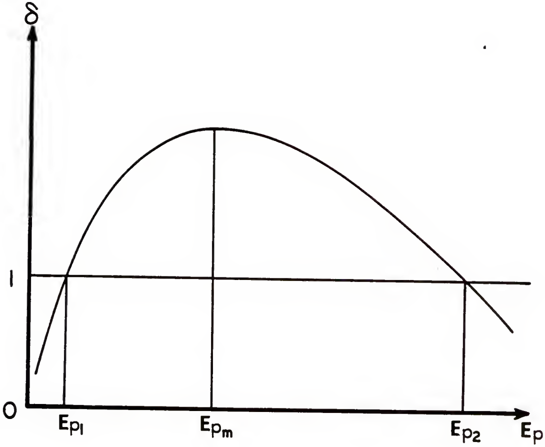

Figure 3. Variation of the secondary electron emission yield as a function of the primary beam energy.

an electric field is produced normal to the surface as a result of the surface positive potential and the diffused negative layer at a depth equal to the electron range. This condition is shown schematically in Figure 4. The electric field strength can be estimated by the energy shift of the Auger peak divided by the electron range, i.e., 10 eV/1000 Å = 10^6 V/cm [79]. From the electrical conduction theory [80], there is little doubt that such a high field can lead to diffusion of alkali ions in the glass. The formation of a sodium deficient layer during 10 keV electron bombardment of a soda-lime-silica glass was demonstrated using SIMS by Gossink and Lommen [81]. Their data indicate that the near surface layer is deficient in sodium and is bounded by a steep rise of the sodium signal at a larger depth. The thickness of this layer increased with electron irradiation time until it became close to the expected maximum range of electron penetration. These data, along with the results of the infrared analysis presented in Figure 2, are direct evidence that field-enhanced diffusion of alkali ions does occur into the bulk of glasses. Therefore, these data support the Lineweaver mechanism, at least in a qualitative sense.

As reported above, a number of workers [10,11,33,36,39,44,45,48] have reported field-enhanced diffusion of mobile ions during AES analysis. For example, Chou et al. [33] observed the diffusion of Cl to the surface of thin oxide on Si during AES analysis. Dawson et al. [44] observed time dependent change in Na, Ca, K, C and O Auger signals from medieval glasses. They attributed the change in Na, K and Ca to field-enhanced migration of cations. Although the simple mechanism postulated by Lineweaver

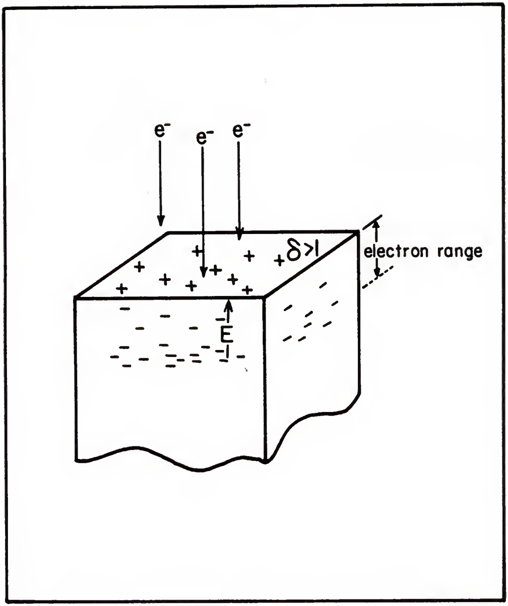

Figure 4. Schematic representation of the electric field produced normal to the surface as a result of the surface positive potential and the diffused negative layer at a depth equal to the electron range.

is attractive, neither an experimental determination of the field strength nor a mathematical model for field-enhanced diffusion has been reported.

Pantano et al. [39] developed an AES technique to improve measurement of alkali concentrations at glass surfaces. They postulated that the alkali disappeared from the surface by diffusion. The rate of disappearance is therefore proportional to the diffusive flux which is equal to the alkali mobility multiplied by the driving force for diffusion. They postulated, therefore, that the high mobility of sodium in glass (which allowed diffusion away from the region of investigation) could be lowered by reducing the temperature of glass. Because of lower mobility, lower signal decay rate would be observed. Their data, reproduced in Figure 5, are consistent with their postulate. An additional significant result is that a characteristic "incubation time" is observed prior to the decay at low temperatures. They interpreted the incubation time on the basis of a time delay before the local temperature (caused by electron beam heating) increased to a critical temperature, T_c, where the alkali mobility was sufficiently high for field-enhanced diffusion. Although there is no doubt that the incident electron beam causes heating, a number of experimental and theoretical studies of beam heating [82-86] show an instantaneous rise in temperature. Therefore, it seems unlikely that it would take so long for the temperature to rise to the critical temperature. For example, Mullendore et al. [87] reported that the AES electron beam caused the temperature of loose titanium powder to rise to the critical temperature for oxygen diffusion (~ 500° C) in less than one second. Thus, a reasonable explanation for the incubation time still remained to be

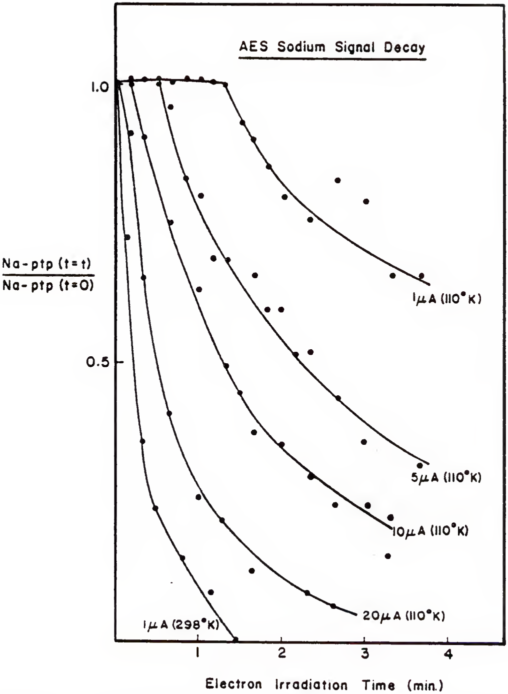

Figure 5. Normalized Auger sodium signal decay from a soda-lime-silica glass at both room temperature and liquid nitrogen temperature using a beam diameter of 500 μm at 3 keV for various levels of beam current (from [39]).

developed. This will be accomplished in the present work. Nevertheless, the incubation time effects allow the use of AES as an analytical technique for structural analysis of glass and ceramics, as demonstrated in this work.

Electron Beam Induced Alkali Volatilization and Desorption

In considering the Auger signal decay of alkali in glass observed with AES, one must also consider alkali volatilization and desorption. This, in a sense, is the opposite of diffusion into the bulk. Insulating materials are expected to be most susceptible to beam heating. Likewise, local beam heating is especially prevalent in Auger microanalysis when high beam energies and small beam sizes are used. The examination of small or thin, unsupported glass specimens presents the most severe beam heating problems because of the difficulty associated with removing the energy deposited by the electron beam. Thus, the analysis of thin glass membranes was unsuccessful due to the melting of holes, as shown in Figure 6(a). Another example is given in Figure 6(b), where a small glass fiber, which was suspended by one end, was observed to soften and collapse when irradiated by an electron beam.

Melting of glass membranes and bending of glass fibers are obviously extreme cases. However, these examples indicate that the electron beam can raise the temperature of the sample higher than the liquidus temperature of the membrane and higher than the softening point of the fibers. From these results, there is little doubt that electron irradiation can induce alkali volatilization when an electron beam with extremely high current density is used, or when a specimen is isolated from a good heat sink.

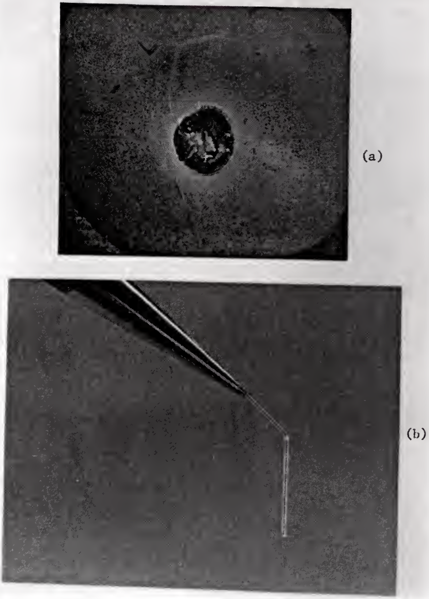

Figure 6. a) Optical microscope photograph of a soda-lime-silica glass membrane showing a hole by melting as a result of electron beam heating. b) A photograph showing collapsed soda-lime-silica glass fiber as a result of electron beam heating. A 3 keV, 100 mA/cm^2 electron beam was used.

Another consequence of electron bombardment is electron stimulated desorption (ESD). It is known that [70] an electron beam can cause desorption of atoms and molecules from a surface as (1) neutral molecules, atoms or fragments, (2) excited neutrals or (3) positive or negative ions. ESD is often discussed only in terms of adsorbates [88-92] and research on desorption from a solid is limited [93,94].

The usual picture of Electron Stimulated Desorption according to Menzel and Gomer [95] and Redhead [96] (MGR model) is that the incident beam excites a bonding electron to an anti-bonding state, and as a result, the effective potential between surface ions and the solid becomes repulsive and the ion desorbs. This model explains many of the distinct characteristics of ESD observed for adsorbates on metal surfaces. The rate of electron stimulated desorption from adsorbates is given by [70]:

$$\frac{d\theta}{dt} = -\frac{i_p\sigma}{e}\theta \qquad (1)$$

where θ is the surface coverage in the binding state which can be desorbed by electron impact, σ is the total desorption cross section, i_p is the electron current density and e is the electronic charge. Therefore, the coverage exponentially decreases with electron bombardment time as follows:

$$\theta = \exp(-t/\tau)$$

where (2)

$$\tau = e/j_p\sigma .$$

In glasses, the electropositive alkali atoms are bound ionically to non-bridging oxygen [80]. Applying the MGR model to alkali desorption from a glass surface, the oxygen-sodium interaction potential has to become repulsive and it is necessary for the oxygen, which is originally ionized negatively, to become positively charged. This means that at least two or three electrons have to be transferred since the oxygen is typically bonded with a charge between -1 and -2. Therefore, the MGR model cannot explain how ESD can occur in glasses.

Knotek and Feibelman [97] have recently developed a new mechanism for ESD, namely, an interatomic Auger de-excitation process. This mechanism can explain the large charge transfer involved in electron stimulated desorption. The desorption mechanism is initiated by production of a core hole on the cation or the anion followed by an interatomic or intraatomic Auger process and desorption of O^+ via a Coulombic repulsion. The loss of oxygen leads to a reduction of surface oxide. The electronic structure of glass is similar to that of maximal valency oxide; therefore, alkali desorption along with oxygen desorption is expected. However, there has been no report of alkali desorption from glasses until the present study.

Research Plan

The above review shows that a fundamental and complete understanding of mechanisms of alkali Auger signal loss has not yet been achieved. This includes the theory of alkali Auger signal decay. Therefore, the present study addresses the following:

1. The parameters describing the rate of alkali Auger signal decay will be clarified and their relative magnitudes will be discussed.
2. Consistent models of the process will be developed mathematically. The experimental results will be compared to the model.

In Chapter II, changes in the alkali Auger signal as a result of electron beam effects were measured for thin glass films deposited on metal. With these samples, the effects on driving force, mobility and electron stimulated desorption were studied. These measurements were coupled with theoretical modeling of alkali diffusion with emphasis on the field-enhanced diffusion.

Although electron stimulated desorption has been observed for a number of gas adsorbates, very little is known about desorption of metal ions from oxide surfaces. In particular, there is a total lack of data for alkali desorption from glass surfaces. Hence, Chapter III is devoted to the investigation of ESD with alkali ions during analysis with AES. Crucial experiments were designed to study ESD. A mathematical model was developed to explain the ESD kinetics and the results of the experiments are discussed quantitatively. The mechanism for ESD of sodium from soda-silica glass was also investigated and a model for sodium desorption was proposed.

On the basis of the work presented in Chapters II and III, a general mathematical description of the Auger signal decay for mobile ions is presented in Chapter IV. The theory is applied to low temperature measurement, and the origin of the incubation time is discussed. Present experimental results are compared with this model.

Finally, in Chapter V, it is shown that the electron beam effects can be used to provide a basis for Auger electron spectroscopy of microstructural as well as compositional analysis. In the present study, binary lithia-disilicate glass was chosen, where controlled nucleation-crystallization of a glass provides a microstructure of uniform small crystals surrounded by a glass matrix. The composition of the crystal is the same as that of bulk glass for this stoichiometric material. Due to the residual phase, compositional variation via any of the mechanisms described may also occur in glass-ceramics during electron bombardment. The electron beam effects on the composite material are discussed.

CHAPTER II
DIFFUSION OF SODIUM DURING ELECTRON BOMBARDMENT

Bombardment of the glass by an electron beam will break bonds to form ion-electron pairs [98] and will raise the local temperature of the material [82-86]. Both effects cause an increase in the alkali ion mobility, which increases the rate of alkali diffusion. While the mobility of the alkali ion is important, a driving force is necessary for diffusion, and this is provided by an electric field. If the charge build-up inside the glass upon electron bombardment is varied by some technique, alkali ion diffusion will change. To change the space charge, glass thin films were deposited on a conducting material so that energetic electrons penetrated through the film and were stopped by the conducting substrate. Therefore, it was postulated that the resultant electric field would be changed when the film thickness was varied. Electron beam heating would also be minimized since good contact to a thermal sink was provided. With these samples, the region of the glass over which forces may act and diffusion will occur is well defined. Therefore, a mathematical model can be developed and compared with the results to determine important parameters such as the electric field.

Experimental Procedure

The measurements reported in this Chapter were from 1000 Å or 2000 Å soda-silica glass films deposited on optically polished stainless steel.

High purity SiO_2 and reagent grade Na_2CO_3 were simultaneously evaporated from an electron beam-heated crucible and a resistively-heated crucible, respectively. During deposition, vacuum was maintained at 5×10^{-5} Torr and the substrate was heated to 300 ° C. Film thicknesses were controlled with a quartz crystal monitor.

For comparison with thin films, bulk glass of Na_2O-$2SiO_2$ was prepared by melting mixtures of reagent grade Na_2CO_3 and high purity SiO_2 at 1400 ° C for 24 hours in a Pt crucible. After casting into a graphite mold, it was annealed at 250 ° C for four hours.

The Auger measurements were made in a Physical Electronics Thin Film Analyzer[†] or a Varian Auger Spectrometer[††] in a residual vacuum pressure of less than 1×10^{-8} Torr. All the samples were irradiated by an electron beam at an angle of 30° (with respect to the plane of the surface) to prevent charging.

In the former instrument (PHI), electron beams with a diameter of 600 μm (defocused beam) and energies up to 3 keV were used. The samples were mounted on a carousel which was cooled with liquid nitrogen. The specimen temperature was monitored with a Chromel-Alumel thermocouple[†††] sandwiched between thin glass slides. The Varian instrument was capable of producing an electron beam with a diameter of 10 μm and energies up to 10 keV. A scanning electron beam was used to more accurately control the electron current density in the Varian spectrometer. The total beam current was measured by a positively biased Faraday cage and beam current densities were calculated based upon the area scanned. Sputter profiling was accomplished using 2 keV Ar^+[†] with the vacuum chamber backfilled to 2×10^{-5} Torr.

[†] CMA 10-155, Perkin Elmer, Physical Electronics Division, Eden Prairie, MN

[††] CMA 981-2707, Varian, Vacuum Division, Palo Alto, CA

[†††] Hoskins Manufacturing Company, Detroit, MI

In studying the change in sodium Auger peak height as a function of electron beam irradiation time, the KLL-sodium peak at 990 eV was monitored by scanning the energy range of 940 to 1020 eV. A derivative signal(EdN/dE) was continuously recorded on a strip-chart recorder.

Results

The Auger spectrum from 1000 Å thick glass film deposited on a stainless steel substrate is shown in Figure 7. The spectrum was taken using a 3 keV electron beam with a total beam current of 5 μA at a liquid nitrogen temperature (~ 110 ° K). A modulation voltage of 5 V peak-to-peak was used. The KLL-sodium peak was again measured. The peak height had significantly decreased, as shown in Figure 7. No elements other than Si, C, O and Na were detected. Using the same procedure, several spots were analyzed on the film. It was found that the relative peak heights for Si, O and Na varied by less than 5% from different analysis sites. Although it is difficult to accurately quantify the Auger data, the glass film composition was estimated (using bulk glass standards) to be 15 ± 5 mole % of Na_2O and 85 ± 5 mole % of SiO_2.

[†] Sputter Ion Gun 04-161, Perkin Elmer, Physical Electronics Division, Eden Prairie, MN

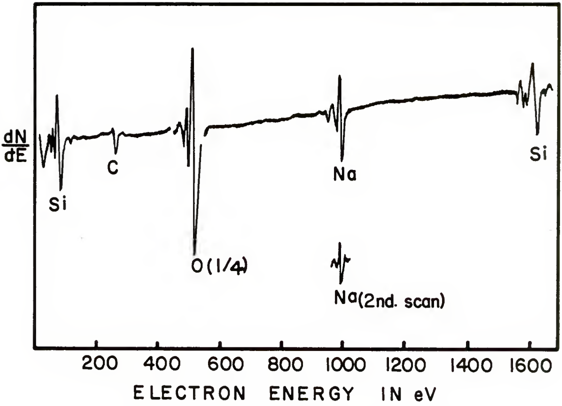

Figure 7. AES spectrum from a 1000 Å thick glass film deposited on a stainless steel substrate, taken using a 3 keV electron beam with a total current of 5 μA at liquid nitrogen temperature (110° K).

The peak heights (normalized to the peak-to-peak height at zero time) for the sodium signal are plotted as a function of beam irradiation time in Figure 8. A 3 keV, 5 x 10^{-3} A/cm^2 electron beam was used to excite the sodium Auger electrons from 1000 Å and 2000 Å films and from bulk glass. The measurements were made at room temperature. The rate of sodium signal decay was strongly dependent upon the film thickness, with significantly slower decay observed for thin films as compared to the bulk glass. The times required for the signal to decay to 50% of its initial value were approximately 5.5, 2.8 and 0.4 minutes for the 1000 Å and 2000 Å glass films and the bulk glass, respectively. When a beam current density of less than 3 mA/cm^2 was used, the sodium signal first increased for one minute and then decayed. Dawson et al. [44] made a similar observation and attributed the effects to removal of a carbon overlayer which inelastically scattered the sodium Auger electrons. In the present case, the carbon signal was observed initially (Figure 7), but it decreased rapidly with electron bombardment. The effect of removal of carbon contamination only delays the time to start sodium Auger signal decay, but the changes in the signal decay rate versus film thickness are the same as those observed at higher beam current densities. This indicated that carbon contamination on the surface can cause significant error in evaluating the surface composition. Therefore, minimal surface contamination was desired for analysis.

The decay rate of the sodium signal was also dependent upon the beam energy. The time dependences of the Na Auger signal from a 2000 Å thick film with energies ranging from 1.5 to 10 keV are shown in Figure 9.

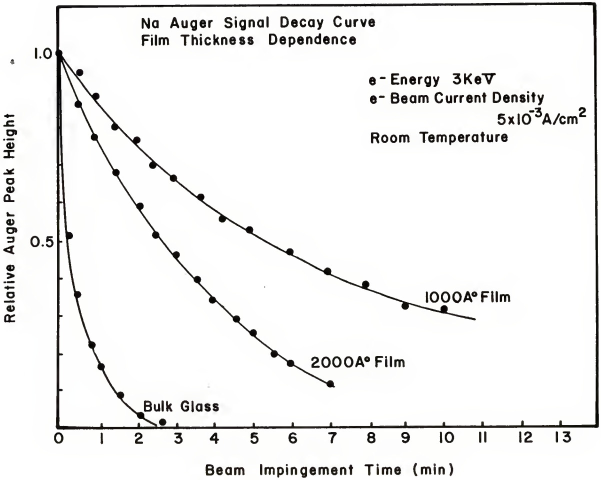

Figure 8. Sodium Auger peak height as a function of beam impingement time and glass thickness for a 3 keV electron beam with a current density of 5 mA/cm^2 at room temperature.

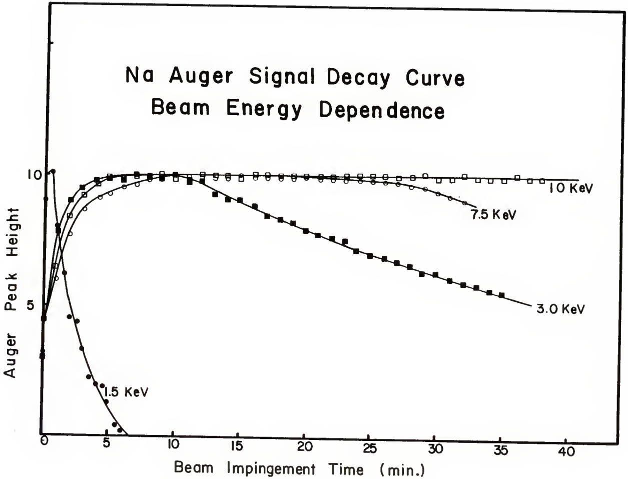

Figure 9. Sodium Auger peak height as a function of beam impingment time from a 2000 Å thick film for energies ranging from 1.5 to 10 keV. The beam current density was 1.4 mA/cm^2 and the analysis was performed at room temperature (300° K).

All the measurements were made at room temperature. In these measurements, a beam current density of 1.4×10^{-3} A/cm^2 was used. As pointed out above, the carbon contamination seriously influenced the measurements and the increase in the sodium signals for the first few minutes resulted from contamination desorption. Nevertheless, the dependence of the sodium Auger signal decay upon beam energy is obvious. For the 1.5 keV electron beam, the sodium decay was quite rapid, while relatively long plateaus were observed for 3.0 and 7.5 keV electrons. Almost no decay was observed from the 10 keV beam. These differences in decay rate will be attributed to changes in the electric field, which is the most important driving force for sodium diffusion.

The results obtained for 2000 Å glass film with 3 keV electrons when the beam current density was varied from 1.4×10^{-3} A/cm^2 to 1.25 A/cm^2, are shown in Figure 10. As the current density was increased, the decay rates increased drastically. According to beam heating models [82-86], the steady state temperature rise is directly proportional to the beam power, which is the product of energy and current. At a constant electron energy, the temperature and therefore the mobility of sodium becomes higher as the current density is increased. Consequently, faster diffusion rate should result. This feature is clearly seen in Figure 10, however, there is no simple relationship (e.g., linear, quadratic, etc.) between the rate of decay and the beam current density.

The sodium mobility in the glass can also be changed by varying the substrate temperature. The sodium Auger signal decays at 110° K and 300° K are compared in Figure 11. Lower temperatures result in a slower decay rate when other factors are constant.

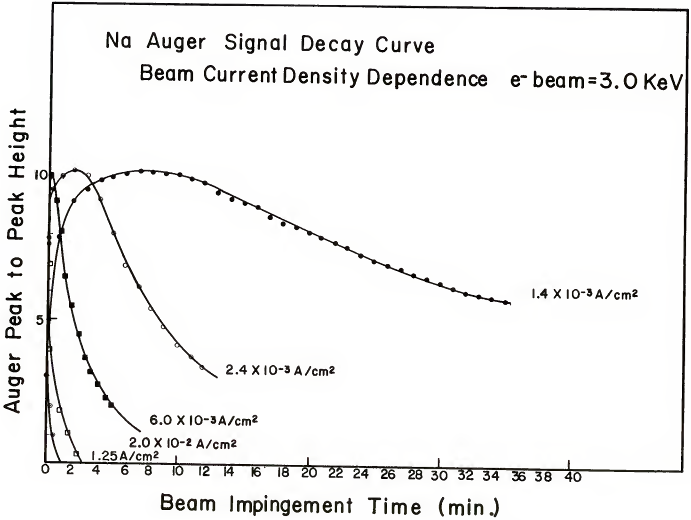

Figure 10. Sodium Auger peak height as a function of beam impingment time from a 2000 Å thick film at room temperature. A 3 keV electron beam was used with the current densities varied between 1.4 mA/cm^2 and 1.25 A/cm^2.
]

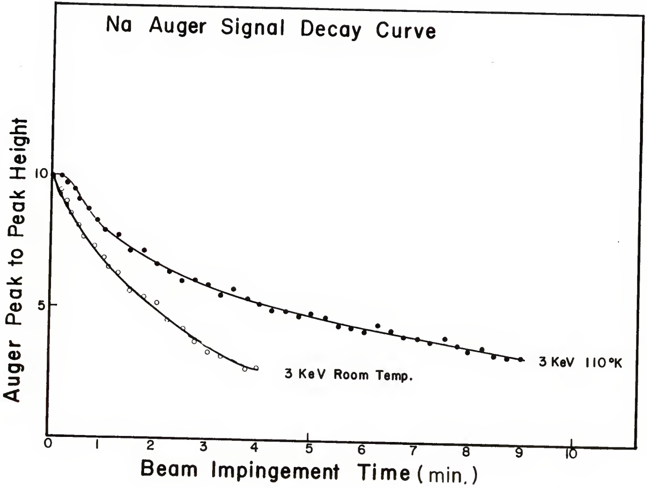

Figure 11. Sodium Auger peak height as a function of beam impingement time from a 1000 Å thick film for a 3 keV electron beam with current density of 5 mA/cm^2 at liquid nitrogen (110° K) and room temperature (300° K).

A Model for Field-Enhanced Diffusion

For thin films, the sodium signal decay rates were strongly dependent upon the electron beam parameters. The decay rate can be controlled by changing either the sodium mobility in the glass or the electric field for diffusion. For thick glass, energetic electrons enter and dissipate their energy by ionization or other electronic excitation of the atoms. They come to rest at some depth, R, within the glass and produce a net negative charge. Theoretical range expression can be obtained by integration of an energy loss expression [99], which is:

$$R = \int_{E=E_0}^{E=0} \frac{1}{dE/dx}\, dE.$$

A simplified range expression was developed by Cosselett and Thomas [100], $R = K\, E_0^n$, where K is a constant and n = 1.2 to 1.7, depending on the definition of range. For low energy electrons, the range expression of Cosslett and Thomas is not precise because of high inelastic scattering. However, it is certain that as the primary energy is increased, the electrons penetrate further into the solid. Typical ranges are a few thousand Angströms, for 3 keV electrons and more than one micron for 10 keV electrons [101]. The sodium Auger signal decay rate was strongly dependent upon the film thickness for a fixed energy, as shown in Figure 8. This was not true in the bulk glass, where the decay rate was almost independent of energy when the current density was kept constant. Therefore, the data shown in Figure 8 can be explained in part by postulating that as the thickness of the film is decreased, the amount of charge trapped also decreased, causing a lower driving force and a lower diffusion rate.

The dependence of the decay rate upon the electron energy shown in Figure 9 is interpreted in the same manner. This is shown schematically in Figure 12. When 1.5 keV electrons enter the 2000 Å glass film, most of the electrons are trapped within the film since the electron range for 1.5 keV is almost the same as the glass film thickness. A space charge is created inside the film and diffusion results. For higher energy beams (e.g., 7.5 or 10 keV), the electrons penetrate through the film and come to rest in the metallic substrate. Therefore, the number of electrons trapped inside the glass film at high energies is significantly lower than at low energies. Correspondingly, diffusion rates are slower for high energy electron bombardment.

The discussion presented above suggests the following model for sodium diffusion during an AES analysis. When a space charge results from bombardment with energetic electrons, the negative charge will be concentrated at a depth about equal to the electron range. A positively charged layer will also exist on the surface since the secondary electron emission yield, δ, is normally greater than unity. A capacitor structure can be used to model the sodium diffusion in the thin film. The model consists of the glass thin film sandwiched by two electrodes, as is illustrated in Figure 13. The diffusion equation including the electric field, F (volt/cm), becomes

$$\frac{\partial c(x,t)}{\partial t} = D\,\frac{\partial^2 c(x,t)}{\partial x^2} - \mu\frac{\partial F(x,t)c(x,t)}{\partial x} \qquad (3)$$

where μ is the mobility of the sodium and D is the diffusion constant. The coordinate perpendicular to the surface is z. For the present case,

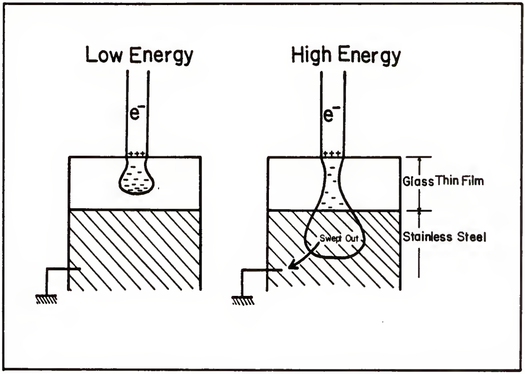

Figure 12. Schematic illustration of the electron beam penetration and the charge accumulation in glass film for low and high energy electrons.

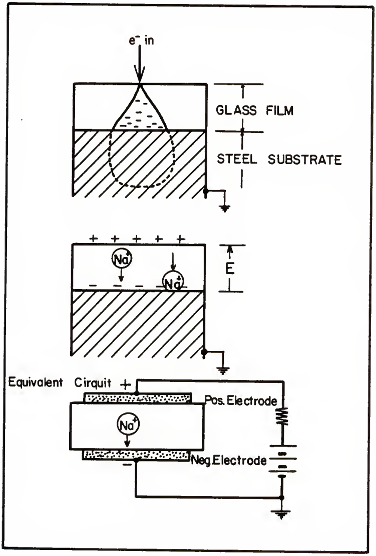

Figure 13. Schematic illustration of the model used to calculate sodium ion diffusion.

it was assumed that F is independent of the time and was taken as an average field strength, F_{av}. Then equation (3) becomes

$$\frac{\partial c(x,t)}{\partial t} = D\,\frac{\partial^2 c(x,t)}{\partial x^2} - F_{av}\mu\,\frac{\partial c(x,t)}{\partial x}\,. \tag{4}$$

From the Einstein relation [102] the mobility of the sodium is expressed by

$$\mu = eD/kT \tag{5}$$

where e, k and T are the electron charge, Boltzman constant and temperature, respectively.

Assuming that the sodium concentration is uniform before the analysis ($t \leqq 0$) leads to the initial condition

$$c(z,t) = c_0 \text{ for } t \leqq 0,\ 0 \leqq z \leqq \ell \tag{6}$$

where C_0 is the initial concentration of sodium in the film and ℓ is the film thickness. We assume that no electron stimulated desorption is occurring at the surface and sodium is physically blocked by the stainless steel at the glass/substrate interface. As a result, there are no fluxes of sodium ions, J, at the surface and interface, i.e.,

$$J = D\,\frac{\partial c}{\partial x} - F_{av}\mu c = 0 \text{ for } x = 0 \text{ and } x = \ell\,. \tag{7}$$

Using these boundary conditions, the equation can be solved analytically. The solution is (see Appendix A)

$$c(x,t) = \frac{c_0 F_{av}\mu\ell\, \exp(F_{av}x/D)}{D(\exp(F\mu\ell/D)-1)} + c_0 16D^2 F_{av}\mu\pi\ell^3\, \exp(F_{av}\mu x/2D)$$

$$X \sum_{m}^{\infty} \frac{\exp((4D^2m^2\pi^2+F_{av}^2\mu^2)t/4D^2\ell^2)m(1-\exp(-F_{av}\mu\ell/2D))}{(4D^2m^2\pi^2+F_{av}^2\mu^2\ell^2)^2}\left(F_{av}\mu \sin\frac{m\pi x}{\ell} + \right.$$

$$\left.\frac{2m\pi D}{\ell}\cos\frac{m\pi x}{\ell}\right). \tag{8}$$

The variation of sodium concentration within the film after electron bombardment can be calculated from this equation.

The sodium surface concentration (i.e., at $z = 0$) as a function of electron bombardment time is

$$\frac{c(0,t)}{c_0} = \frac{F_{av}\mu\ell}{D(\exp(F_{av}\mu\ell/D)-1)} + 16D^2 F_{av}\mu\pi\ell^3$$

$$X \sum_{m}^{\infty} \frac{2m\pi D \exp((4D^2m^2\pi^2+F_{av}^2\mu^2)t/4D^2\ell^2)m(1-\exp(F_{av}\mu\ell/2D))}{\ell(4D^2m^2\pi^2+F_{av}^2\mu^2\ell^2)^2}. \qquad (9)$$

Therefore, the normalized Auger signal can be approximated by equation (9), since the Auger escape depth of sodium is very small [66] relative to the film thickness.

Discussion

A Model Calculation and Estimation of Field Strength

A theoretical model has been presented for describing sodium Auger signal decay in the glass thin film. The model considers only diffusion influenced by the electric field which was assumed to be uniform throughout the film. In a quantitative comparison of this model with the expermental data, the field strength, F_{av}, can be treated as an adjustable parameter such that calculated curves give a best fit with experimental data. As discussed before, local heating by the electron beam causes the temperature of the substrate to increase, thereby increasing the mobility. This beam heating effect is implicitly included in the model through the diffusion constant.

As has been shown in a number of studies of beam heating, the local temperature rises almost instantaneously [82-86] and reaches a steady state value in the thin film. The local temperature has been measured by a thin thermocouple on a glass microscope slide and temperature rises of 150° to 250° C were obtained [103] when a 3 keV electron beam with a beam current density of 1 mA/cm^2 was used. Therefore, for analysis with the carousel at room temperature, a diffusion constant of ~ 3.5×10^{-15} cm^2/sec (corresponding to the constant at 200° C [104]) is taken as an appropriate value. Calculated results from equation (9) are plotted in Figure 14, where best fits to the experimental data presented in Figure 8 are given. The average field strengths determined from these calculations were 2.2×10^4, 3.9×10^4 and 1.2×10^5 V/cm for 1000 Å and 2000 Å films and bulk glass, respectively. For the bulk glass, the electron range was calculated (3000 Å for 3.0 keV electron beam [101]) and used as the equivalent film thickness. Therefore, the estimated field strength in the bulk glass may vary by a factor of one to five, depending on the range determined. However, the calculated field strength does show a consistent trend with film thickness.

The surface charging can be estimated from shifts in energy of the Auger peak [79]. For the 2000 Å film, peak shifts of 1 ± 0.5 eV were measured for a 3.0 keV electron beam. Assuming this charge acts over the 2000 Å film, the field strength is estimated to be 5×10^4 V/cm. This is approximately the same as the field strength calculated from the model. The energy of the sodium Auger transition from bulk glass shifted from 3 to 6 eV, again giving a field strength of 10^5 to 2×10^5 V/cm,

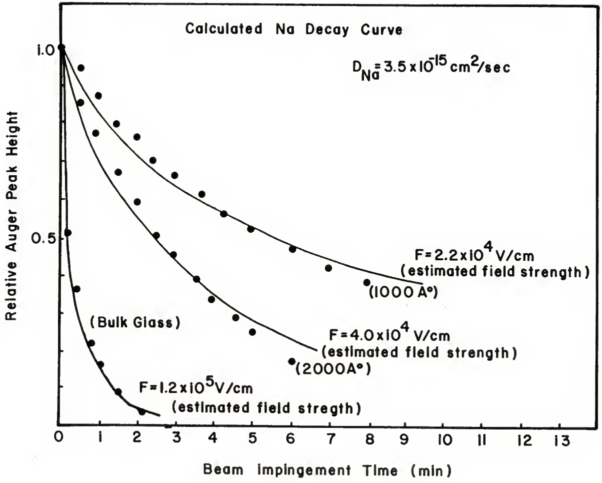

Figure 14. Calculated sodium decay curves (solid lines) that are best fit to the experimental data shown in Figure 8.

assuming an electron range of 3000 Å; this is reasonably consistent with the value derived by curve fitting the experimental results. This coincidence suggests that our assumption of a uniform average field is good in this case. However, the field in a bulk sample may be significantly different. For example, the electron range in a bulk film is only an average value and the resulting charge will straggle over a large distance about this value (e.g., ± 500 Å for a 3 keV electron in SiO_2 [105]). In addition, a non-uniform distribution of sodium ions, electrons and holes may exist. Therefore, the diffusion equation has to be solved under non-uniform electric field conditions (equation (3)). This cannot be done until a detailed charge distribution is known.

Local heating by the electron beam has been approximated in this case based upon experience [103]. This is only a crude estimate. Beam heating was expected to vary not only when the current density was changed, but when the geometry was changed. The sodium Auger signal decays at 110°K and 300°K (Figure 11) were not significantly different. This is because the film is in direct contact with a good thermally conducting material and heat is dissipated well, even at room temperature. The temperature, thereby the mobility, may not be as high as those estimated (i.e., 200°C). Therefore, the field strength in the film should be higher in order to provide a larger driving force and diffusion rate. However, the calculation does provide a lower limit on possible field strength and it indicates that a very high field exists in the film.

Sodium Depth Profile

In the above discussion, the sodium Auger signal decay was dependent upon the electron beam energy, current density and substrate temperature. It was found that the field induced by the electron beam was about 10^5 V/cm. In such a high electric field, there is no doubt that the sodium will move [80,106]. According to the model, the sodium ions are driven into the thin glass but are physically blocked at the interface between the film and the stainless steel. Thus, accumulation of the sodium at the interface is expected. This is shown by the concentration versus depth curves calculated from equation (7). The calculated sodium concentrations versus depth in the film after irradiation by an electron beam is shown in Figure 15. Sodium is depleted near the surface and accumulates at the interface. This accumulation is enhanced by a longer irradiation time.

To test this predicted accumulation, the sodium concentration versus depth was measured by Ar^+ sputtering. A depth profile after irradiation of the surface of a 1000 Å glass film is shown in Figure 16. A 3 keV, 1×10^{-2} A/cm^2 electron beam was scanned over ~ .2 mm^2 to obtain homogeneous irradiation of the film. After the signal decayed to 25% of its maximum peak height, the sodium was sputter profiled. A 3 keV, 1×10^{-3} A/cm^2 primary electron beam was used during sputtering, but only sodium and iron Auger signals were recorded. The beam bombardment time was no more than 10 seconds at each depth profile concentration point. As shown in Figure 16, lower concentrations of sodium were observed in the middle of the film, and a large accumulation was again detected at the interface. The depth profile from an unirradiated area of the 1000 Å film is also shown for the

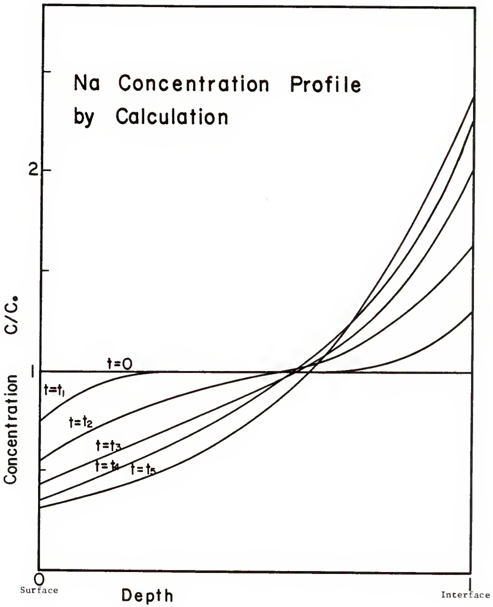

Figure 15. Calculated sodium distribution in the film after electron beam impingement for time t, when $t_1 = 0 < t_2 < t_3 < t_4 < t_5$.

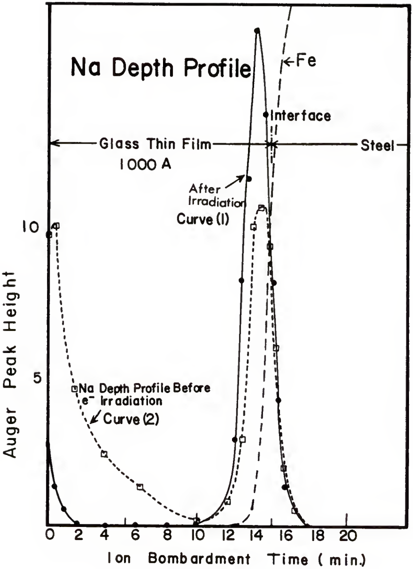

Figure 16. Sodium concentration depth profile in the 1000 Å glass film from an unirradiated area (shown by dotted curve) and an irradiated area (shown by solid curve). Iron signal profile is shown by broken line curve.

comparison. Higher accumulation at the interface for the irradiated area indicates that some of the sodium migrates into the solid due to the surface electron bombardment.

However, the depth profile of the unirradiated area departs significantly from the expected uniform concentration distribution. This is thought to result from sodium diffusion induced by ion bombardment. McCaughan et al. [107] observed that Ar^+ bombardment caused migration of sodium ions in SiO_2. An accumulation of sodium at the SiO_2/Si interface was observed and the sodium depth profile was similar to Figure 16. Although the interaction of ions with the solid is much more complicated than that of electrons, they explained the result by considering an ion neutralization process [108] at the surface. Incoming low energy Ar^+ are neutralized within a few Angstroms of the SiO_2 surface. This leads to a build-up of a positive charge on the surface, which causes sodium diffusion. In the present instance, the sodium diffuses more than the Auger escape depth, resulting in a lower Auger signal intensity. The glass/stainless steel interface blocks sodium diffusion and an accumulation results.

In each depth profiling step, the electron beam was exposed for a short time (less than 10 seconds) to observe the sodium concentration. In this case the electric field is instantaneously established and the sodium would move into the bulk under the field. However, the estimated decay within 10 seconds is only ~ 3% at 1×10^{-3} A/cm^2, in addition, the sodium may relax back towards the surface after the electron beam was turned off. Thus, the 10 seconds of electron beam exposure is not expected to cause a severe depletion of sodium in the middle of the film.

In spite of the ion beam effect, the depth profiles in Figure 16 still have a discrepancy. If only electron beam induced diffusion occurred during Auger measurements, the area under the depth profile should be proportional to the total amount of the sodium in the film. By comparing the area under the two profiles, it is apparent that the amount of sodium ions from the irradiated area (curve (1)) is smaller than that from the unirradiated area (curve (2)). This indicates that some of the sodium ions are lost during the surface irradiation, i.e., electron stimulated desorption has occurred.

In this case, the effect of electron stimulated desorption should be taken into account in the model. However, as will be shown in Figure 28 (Chapter III), the electron stimulated desorption becomes important only when the beam current is high (e.g., >1 mA/cm^2). Thus, the field strength calculated from the present model is still valid. The importance of electron stimulated desorption is substantiated by the data in Figure 10. Anomalously, high decay rates observed at high beam current densities (e.g., 2×10^{-2} A/cm^2 or 1.25 A/cm^2) are attributed to electron stimulated desorption. Therefore, we could not correlate the Auger signal decay rate with the beam current density. Both field-enhanced diffusion and electron stimulated desorption are occurring simultaneously to cause the sodium signal decay. Electron stimulated desorption will be discussed in the next chapter.

Summary

1. Change in the sodium Auger signal due to electron bombardment has been studied using thin films of soda-silica glass deposited on a stainless

steel substrate. With these samples, the effects of electric field, mobility and temperature have been demonstrated.

2. The amounts of charge trapping and local heating are a strong function of the beam parameters for thin films. For example, the time required for the sodium Auger signal to decay to 50% of its initial value increased as the beam energy was increased, or as the current density was decreased.
3. The rearrangement of sodium due to charge trapping was modeled using a configuration similar to a capacitor. A diffusion equation, including the electric field, was solved. The calculated and experimental data agree well and indicate that fields of ~ 10^5 V · cm^{-1} exist during analysis.
4. The model was also used to calculate the distribution of sodium with depth, but the calculated distribution disagreed with the experimental sputter profiling data. This probably results from redistributions during ion bombardment for sputter profiling. Therefore, care has to be taken in interpreting depth profiles.
5. Electron stimulated desorption of sodium occurs during AES analysis.

CHAPTER III
DESORPTION OF SODIUM DURING ELECTRON BOMBARDMENT

As stated in the previous chapter, electron stimulated desorption (ESD) is one of the mechanisms for alkali Auger signal loss during analysis with AES. Upon electron bombardment, some of the sodium atoms are desorbed into the vacuum from the surface and others diffuse into the bulk at the same time. Therefore, the Auger signal decay is more complicated, since both diffusion and desorption have to be considered simultaneously. The electron stimulated desorption of sodium was studied in the AES-SIMS system with experimental conditions similar to those of conventional AES analysis. A phenomenological model was developed, in which diffusion and desorption are simultaneously taken into account. The results are then compared with the model and an ESD cross section for sodium was evaluated. A mechanism for sodium desorption from glass was also determined by applying a recently developed ESD model where Auger de-excitation of a core hole causes desorption [97 ,109].

Experimental Procedure

A Na_2O-$2SiO_2$ glass was prepared in a manner similar to that described in Chapter II. Glass fibers with a diameter of 400 to 800 μm were drawn from the molten glass state. The fibers were then held with a clip attached to a carousel. In order to create a new clean surface, the fibers were fractured in the vacuum chamber at a pressure of 1 x 10^{-9} Torr just prior to the ESD experiment.

The experimental system incorporated a UTI quadrupole mass filter[†] with a 3M prefilter,[††] AES single pass CMA,[†††] a 3M minibeam ion gun[††††] and a sample manipulator.[†††††] The secondary ion mass spectrometry (SIMS) and Auger electron spectrometry (AES) can be used simultaneously without changing the sample location. Therefore, in the present ESD experiment, fractured surfaces were exposed to the scanning electron beam from the coaxial gun in the CMA, and desorbed ions were detected by the quadrupole mass filter.

In studying ESD of sodium from glass surfaces, the quadrupole mass filter was tuned to m/e = 23 (Na^+) and the intensity was recorded as a function of electron bombardment time. During measurements, the ion gauge was off. The background signal at m/e = 23 (such as Na ions from the W filament of the electron and ion guns, Na ions from the vacuum chamber walls, etc.) was eliminated by setting the signal discriminator[††††††] at the background signal level.

Primary electron energies of 500 to 4000 eV and beam current of 10^{-8} to 10^{-6} A were used during most experiments, since these are the ranges used in typical Auger analyses [1]. The electron beam current density was determined by dividing the total beam current by the area scanned. Auger measurements were made simultaneously.

[†] UTI 100C, UTI, Sunnyvale, CA

[††] 3M Model 610 SIMS Prefilter, 3M Company, St. Paul, MN

[†††] CMA 15-110, Perkin Elmer, Physical Electronics Div., Eden Prairie, MN

[††††] Minibeam Ion Gun, 3M Company, St. Paul, MN

[†††††] PM-600XYZTRC, Huntington Mechanical Lab, Inc., Mountain View, CA

[††††††] Model 9302, Amplifier-Discriminator, ORTEC, Inc., Oak Ridge, TN

A threshold energy measurement for desorption of sodium was carried out by rearranging the electronics cabling of the Auger electron spectroscopy unit and the mass spectroscopy unit, as shown in Figure 17. The negative sweep voltage normally used to drive the cylindrical mirror analyzer was used as a sweepable accelerating voltage for the electron beam. In this case, the energy of primary electrons can be directly read from the digital panel meter housed in the Auger controller.[†] The beam current was maintained in the 10^{-8} A range by adjusting the emission current as the beam voltage was changed.

Results

Electron stimulated desorption spectra from glass surfaces are shown in Figure 18(a) and (b). The sample was exposed to a pressure of (a) 10 minutes at 1×10^{-9} Torr , and (b) 90 minutes after an *in situ* fracture. The quadrupole mass filter was scanned from m/e = 1 to 50. Major peaks observed in the spectra are 1, 16, 17, 19, 23, 28 and 44 in mass to charge ratio (m/e), which are identified as H^+, O^+, OH^+, F^+, Na^+, CO^+ and CO_2^+, respectively. It should be noted that all peak intensities vary with electron beam bombardment time and the relative intensities are strongly dependent upon the time of exposure to the electron beam. Therefore, the spectra shown in Figure 18 are only representative of typical data but do indicate which ions are representative of the original fracture surface.

[†] 11-500A Auger System Control, Perkin Elmer, Physical Electronics Division, Eden Prairie, MN

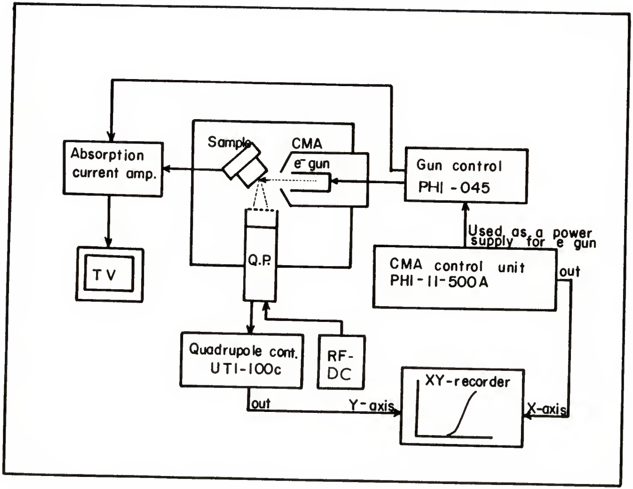

Figure 17. Experimental configuration for threshold energy measurement of ESD.

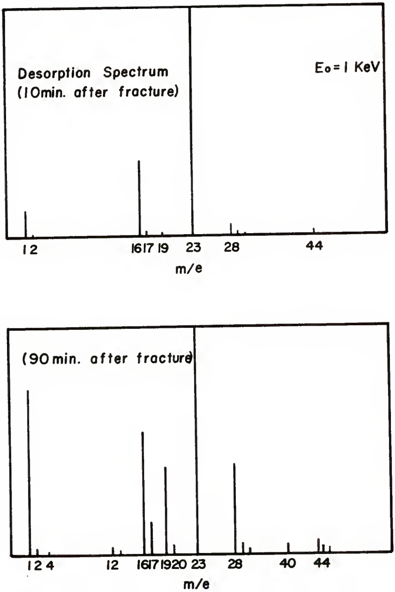

Figure 18. ESD spectra from a soda-silica glass surface exposed to a pressure of 1×10^{-9} Torr for 10 minutes. (a) For 90 minutes, (b) after an *in situ* fracture. A 1 keV, 1 mA/cm^2 electron beam was used.

The relatively high peaks at m/e = 1, 17, 19 and 28 in Figure 18(b) indicate that the fracture surface is partially covered with H_2, H_2O and CO. Partial pressure analysis with the mass filter indicated that H_2, H_2O and CO were the major residual gases at 1×10^{-9} Torr but no F compounds were observed. These peaks are considerably smaller in the spectrum taken 10 minutes after the fracture (Figure 18(a)) and peaks for m/e = 1, 16 and 23 are dominant.

This observation substantiates that a clean surface is conserved for more than 10 minutes without severe contamination by the residual gas in the vacuum chamber. Therefore, all the ESD experiments discussed in this chapter were made within 10 to 20 minutes after creating a new surface.

Figure 19 shows a desorption rate profile of m/e = 16 (O^+) and 23 (Na^+) signals as a function of electron bombardment time. A 1 keV scanning electron beam with a beam current density of 1 mA/cm^2 was used. Note that the desorption rate for m/e = 23 (Na^+) rises initially for the first 20 seconds. This is followed by a monotomic decrease at longer electron bombardment times. For m/e = 16 (O^+), the initial rise was not observed. Instead, the rate was nearly constant for 20 seconds and then decreased. The absorption current did not vary significantly with time during electron beam bombardment, suggesting that charging of the specimen did not occur.

Similar desorption curves were obtained for m/e = 23 (Na^+) for energies of 0.5, 1, 2 and 4 keV beam current densities varying between 10^{-4} and 10^{-2} A/cm^2. These data were normalized at the maximum desorption rate for each energy and are plotted versus electron dose (the product of beam current density and electron bombardment time) in Figure 20(a), (b), (c) and (d)

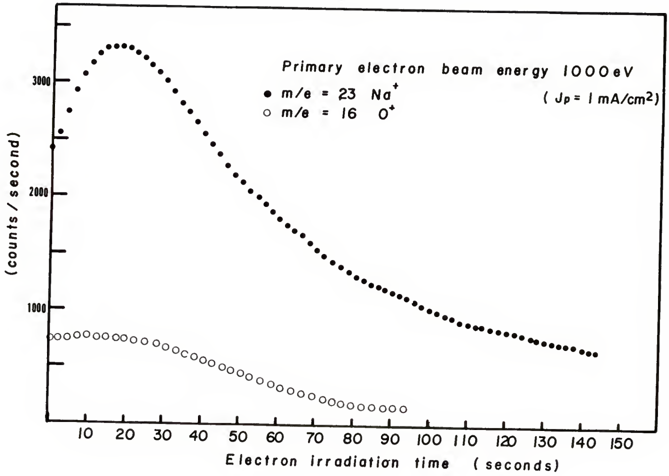

Figure 19. A desorption rate profile of m/e = 16 and 23 signals from the soda-silica glass surface as a function of electron beam bombardment time. A 1 keV, 1 mA/cm^2 electron beam was used.

for 0.5, 1, 2 and 4 keV electrons, respectively. Plotting dose on the abscissa, the experimental data fall on a single line for a fixed energy when the beam current was varied from 10^{-4} to 10^{-3} A/cm^2. In all the results, the desorption rate curves consist of an initial rise followed by a monotonic decrease. When the primary beam energy was increased, the electron dose necessary to reach the maximum rate was shifted to a higher value and the rate of decay after the maximum was decreased.

The maximum desorption rates versus beam current densities between 10^{-4} and 10^{-3} A/cm^2 (at 2 keV) are shown in Figure 21. The rate becomes larger as the current density increases, but the relationship is not linear. Similar results were observed at other primary electron energies.

The oxygen desorption signals (m/e = 16) were also monitored with beam current densities ranging from 10^{-3} to 10^{-2} A/cm^2 (at 2 keV). The normalized signals versus electron dose are shown in Figure 22. Again, most of the data form a single line except for the highest beam current density. For beam current densities of 10^{-3} A/cm^2, the desorption rate does not vary up to ~ 3×10^{-2} coulomb/cm^2 and the rate subsequently becomes lower, similar to the sodium desorption rate at 2 keV. The oxygen KLL Auger signal was also monitored during the ESD experiment. The peak height decreased with increasing irradiation dose, as shown in Figure 23. The oxygen Auger electron escape depth is at least several times larger than the ion escape depth in ESD [66,88]. Therefore, the rate of decrease of the AES signal is slower than for the ESD signal.

Although the data show that the electron beam desorbs sodium and oxygen from glass, the initial rise in the sodium desorption rate cannot

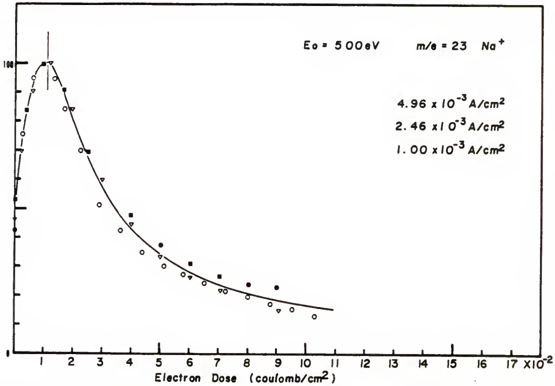

Figure 20(a). A desorption rate profile of m/e = 23 (Na$^+$) signal from the soda-silica glass surface as a function of electron dose. Figures (a), (b), (c) and (d) are for the energies of 0.5, 1, 2 and 4 keV, respectively, with varying beam current densities shown in figures.

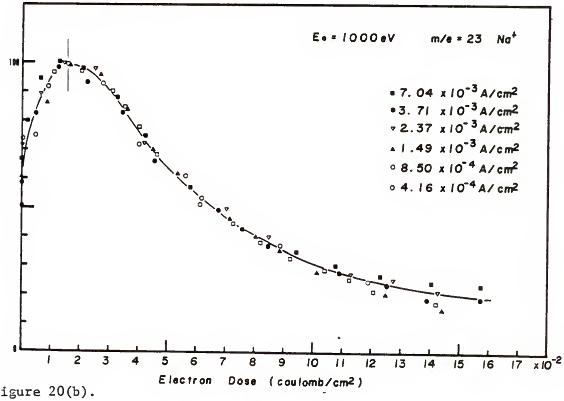

Figure 20(b).

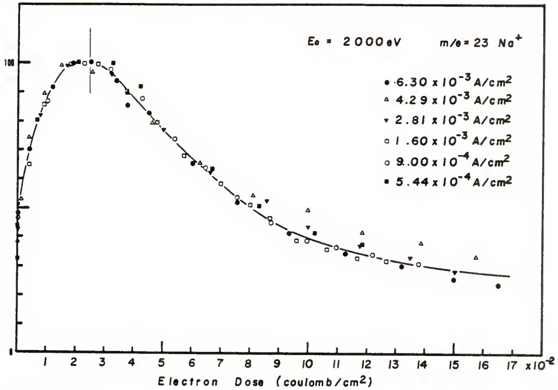

Figure 20(c).

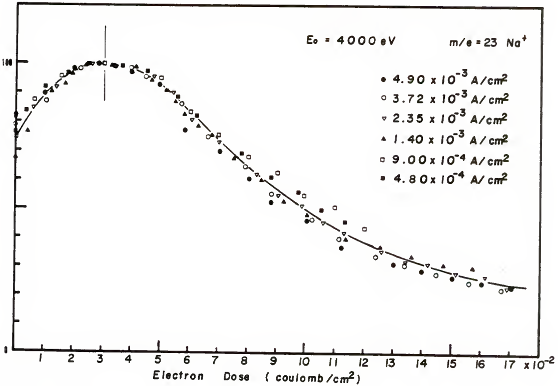

Figure 20(d).

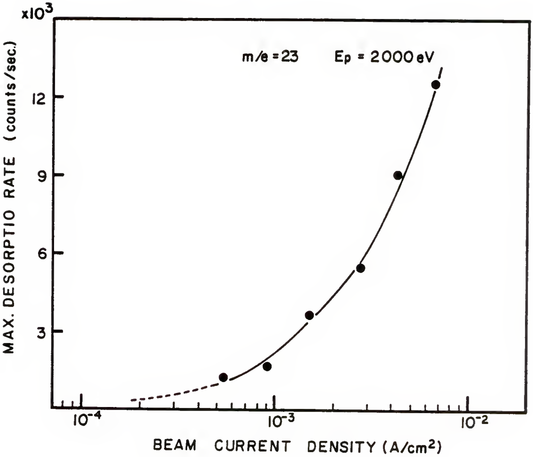

Figure 21. A plot of maximum desorption rates of sodium from the soda-silica glass surface as a function of beam current density at 2 keV.

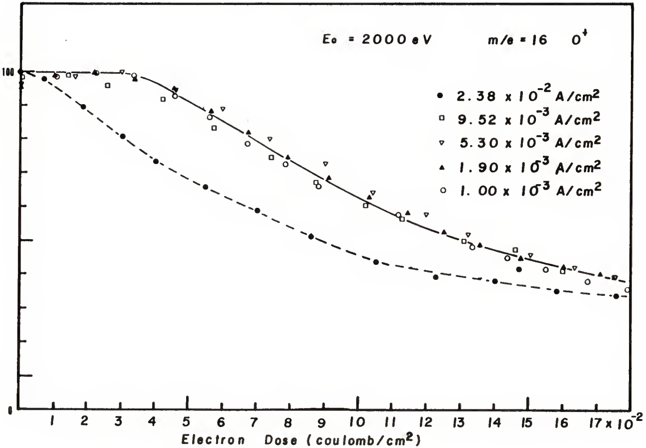

Figure 22. A desorption rate profile of m/e = 16 (O^+) signals from the soda-silica glass surface as a function of electron dose at 2 keV.

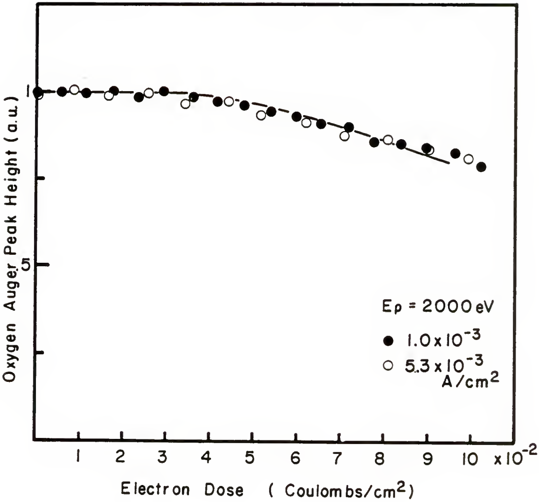

Figure 23. A plot of oxygen (KLL) Auger peak height from the soda-silica glass surface as a function of electron dose at 2 keV.

be explained by a conventional ESD mechanism, where the rate of desorption is expressed by an exponential decay (equation (2)). Neither the variation of rate of desorption with time, nor the non-linearity of rate with beam current density can be explained. This is because both electron stimulated desorption and diffusion processes are simultaneously occurring at the surface. A phenomenological model was developed and solved mathematically. The model is compared with experimental results in the next section.

Phenomenological Model of ESD on Glass Surface

A Model

The proposed model is similar to one used by Kirby et al. [25, 26] to explain Auger data for oxygen or carbon monoxide adsorbed on a silicon surface, where the adsorbed molecular species are dissociated under the electron beam. The dissociated species may then desorb or diffuse into the silicon. By analogy, the following process is considered. When the electrons strike the glass surface, they may break the ionic non-bridging oxygen-sodium bonds [98]. Ion pairs of an oxygen ion and a sodium ion are created at the surface. The oxygen ion traps a hole in a non-bonding 2p orbital [68,110] and the sodium is no longer bound to the oxygen [68]. Such defects are reported in studies of radiation damage in soda-silica glass [111]. Unless there is some mechanism to stabilize the defect, the bond will reform and the defect will disappear. At a surface, however, a stress relaxation of broken bonds may stabilize the defect [112]. Thus, the sodium may be desorbed into the vacuum or diffused into the bulk. The desorption occurs via Coulombic repulsion with O^+, which is produced by interatomic Auger de-excitation or intraatomic Auger de-excitation processes [97 ,109] (see detailed discussion in a later section). Sodium diffusion proceeds under the influence of the electric field.

Mathematical Formulation of Model

The processes considered above are described in the following diagram.

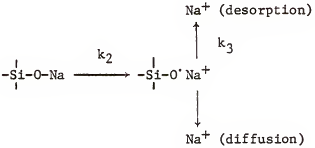
Na$^+$ (desorption)
k_3
k_2
$-\overset{|}{\underset{|}{\mathrm{Si}}}-\mathrm{O}-\mathrm{Na}$
$-\overset{|}{\underset{|}{\mathrm{Si}}}-\mathrm{O}^{\cdot}\,\mathrm{Na}^+$
Na$^+$ (diffusion)

where $-\overset{|}{\underset{|}{\mathrm{Si}}}-\mathrm{O}-\mathrm{Na}$ represents the state in which the sodium and non-bridging oxygen is ionically bound, and $-\overset{|}{\underset{|}{\mathrm{Si}}}-\mathrm{O}^{\cdot}\ \mathrm{Na}^+$ represents the state in which the O-Na bond is broken by electron bombardment and a hole is trapped at O.

In order to formulate these processes mathematically, the following parameters are defined:

k_2 = a constant associated with the rate of conversion of sodium from $-\overset{|}{\underset{|}{\mathrm{Si}}}-\mathrm{O}-\mathrm{Na}$ to $-\overset{|}{\underset{|}{\mathrm{Si}}}-\mathrm{O}^{\cdot}\ \mathrm{Na}^+$.

k_3 = a constant associated with the rate of desorption.

The concentration of the atoms or ions is time dependent as defined by:

$C_1(t)$ = surface concentration of Na bonded to non-bridging oxygen at $-\overset{|}{\underset{|}{\mathrm{Si}}}-\mathrm{O}-\mathrm{Na}$,

and

$C_2(t)$ = surface concentration of Na^+ ion after conversion at $-\overset{|}{\underset{|}{\mathrm{Si}}}-\mathrm{O}^{\cdot}\mathrm{Na}^+$. These have the following unit: number of atoms (including ions)/cm^2.

If we assume that the conversion is a first order reaction, the rate equations for the system are

$$\frac{d}{dt} C_1(t) = -k_2 C_1(t) \tag{10}$$

$$\frac{d}{dt} C_2(t) = -k_3 C_2(t) - \frac{d}{dt} n_b(t) + k_2 C_1(t) \tag{11}$$

where the number of atoms which have diffused into the bulk is given by $n_b(t)$.

In evaluating the bulk diffusion term, a one-dimensional field-enhanced diffusion equation can be applied as discussed in Chapter II.

$$\frac{\partial}{\partial t} C_b(z,t) = D \frac{\partial^2}{\partial z^2} C_b(z,t) - F\mu \frac{\partial}{\partial z} C_b(z,t) \tag{12}$$

where F and μ are electric field strength and mobility, respectively. Here z is the distance perpendicular to the surface. A quantity, $C_b(z,t)$, is the bulk concentration with a dimension of number of atoms/cm^3. A parameter, p, with a dimension of cm^{-1} is introduced, where p is a distance at which sodium is considered to be bulk sodium, as opposed to surface sodium available for ESD or Auger measurement. The boundary condition for equation (12) is taken as

$$C_b(0,t) = p\, C_2(t). \tag{13}$$

The intital conditions are

$$C_1(0) = C_{01} \quad \text{and} \quad C_2(0) = 0 \tag{14}$$

where C_{01} is the number of sodium atoms bonded to non-bridging oxygen before electron bombardment.

In Appendix B, we obtain the solution of equation (12) as

$$C_b(z,t) = \frac{pz}{2\sqrt{\pi D}} \cdot \exp\left(\frac{F\mu}{2D} z - \frac{(F\mu)^2}{4D} t\right)$$
$$X \int_0^t C_2(t') \cdot \exp((F\mu)^2 t'/4D) \cdot (t-t')^{-3/2} \cdot \exp(-z^2/4D(t-t'))dt'. \tag{15}$$

The number of atoms in the bulk (semi-infinite solid) is then given by

$$n_b(t) = \int_0^\infty C_b(z,t)dz \tag{16}$$

$$= \frac{p}{2\sqrt{\pi D}} \cdot \exp\left(-\frac{(F\mu)^2}{4D} t\right) \cdot \int_0^t C_2(t') \cdot \exp\left(\frac{(F\mu)^2}{4D} t'\right) \cdot (t-t')^{-3/2} \cdot Q(t,t')dt' \tag{17}$$

where

$$Q(t,t') = 2D(t-t') \left\{1 + \frac{(t-t')^{1/2}}{\sqrt{D}} F\mu \cdot \exp\left(\frac{(F\mu)^2}{4D}(t-t')\right) \cdot \mathrm{Erfc}\left(\frac{F\mu}{2\sqrt{D}} (t-t')^{1/2}\right)\right\}. \tag{18}$$

Differentiating with respect to t, we obtain

$$\frac{dn_b(t)}{dt} = -\frac{p\sqrt{D}}{2\sqrt{\pi}} \cdot \int_0^t C_2(t') \cdot (t-t')^{-3/2} \cdot \exp\left(-\frac{(F\mu)^2}{4D}(t-t')\right)dt'. \tag{19}$$

Substituting (19) and the solution of (10) into (11), we obtain the coupled integro-differential equation for the model, as solved below.

Solution

The exponential term in equation (19) may be expanded by a series approximation and we integrate by parts using the conditions of (13) and (14). We obtain

$$\frac{dn_b(t)}{dt} = -\frac{p\sqrt{D}}{2\sqrt{\pi}} \cdot \sum_{n=0}^{\infty} \int_0^t \frac{dC_2(t')}{dt'} \cdot \frac{(-1)^n}{n!} \cdot \left(\frac{(F\mu)^2}{4D}\right)^n \frac{(t-t')^{n-1/2}}{n-1/2}\, dt'. \qquad (20)$$

Inserting (20) into (11), the Laplace transform of equation (11) is obtained as

$$s\,\bar{C}_2(s) = -k_3\bar{C}_2(s) - \mathcal{L}\{\frac{dn_b(t)}{dt}\} + \frac{k_2C_{01}}{s+k_2} \qquad (21)$$

where $\bar{C}_2(s)$ is the Laplace tranformation of the concentration $C_2(t)$, i.e.,

$$\bar{C}_2(s) = \mathcal{L}\{C_2(t)\}. \qquad (22)$$

Using the convolution theorem in the Laplace transformation, equation (21) is reduced to (Appendix C),

$$s\,\bar{C}_2(s) = -k_3\bar{C}_2(s) + \frac{p\sqrt{D}}{2\sqrt{\pi}} \sum_{n=0}^{\infty} \{\frac{(-1)^n}{n!} \cdot \left(\frac{(F\mu)^2}{4D}\right)^n \cdot \frac{1}{n-1/2} \cdot \frac{\Gamma(n+1/2)}{s^{n-1/2}}\,\bar{C}_2(s)\} + \frac{k_2C_{01}}{s+k_2} \qquad (23)$$

where $\Gamma(n+1/2)$ is the Gamma function.

Solving equation (23) for $C_2(s)$, we obtain

$$\bar{C}_2(s) = k_2C_{01}(s+k_2)^{-1} \cdot [s+k_3 - \frac{p\sqrt{D}}{2\sqrt{\pi}} \cdot \sum_{n=0}^{\infty} \{\frac{(-1)^n}{n!}\left(\frac{(F\mu)^2}{4D}\right)^n \cdot \frac{1}{n-1/2}\, \frac{\Gamma(n+1/2)}{s^{n-1/2}}\}]^{-1}. \qquad (24)$$

If we replace the infinite summation in equation (24) by a partial summation, which is taken large enough to minimize the error, we obtain

$$\bar{C}_2(s) \simeq k_2 C_{01}(s+k_2)^{-1} \cdot [s+k_3 - \frac{p\sqrt{D}}{2\sqrt{\pi}} \cdot \sum_{n=0}^{K} \{\frac{(-1)^n}{n!} \cdot \frac{(F\mu)^2}{4D} \cdot \frac{1}{n-1/2} \cdot \frac{\Gamma(n+1/2)}{s^{n-1/2}}\}]^{-1}. \tag{25}$$

We can then write

$$\bar{C}_2(s) \simeq \frac{k_2 C_{01} s^K}{\sqrt{s}\, M(s)} \tag{26}$$

where

$$M(s) = (s+k_2) \cdot (s^{K+1/2} + k_3^{K-1/2} + \sum_{n=0}^{K} \alpha_n \cdot s^{K-n}). \tag{27}$$

The expression for M(s) can be written

$$M(s) = \prod_{j=1}^{K+3} (\sqrt{s} + g_j) \tag{28}$$

where the g_j are constants to be determined. Using equation (27) and rearranging, we can write equation (26) as

$$\bar{C}_2(s) \simeq \sum_{j=1}^{K+3} \frac{B_j}{\sqrt{s}(\sqrt{s}+g_j)} \tag{29}$$

where the B_j are constants to be determined. The inverse Laplace transform of each term is given by [113]

$$\mathcal{L}^{-1} \frac{1}{\sqrt{s}(\sqrt{s}+g)} = \mathcal{F}(g\sqrt{t}) \tag{30}$$

where

$$\mathcal{F}(g\sqrt{t}) = \exp(g^2 t) \cdot \mathrm{erfc}(g\sqrt{t}). \tag{31}$$

It is difficult to use this solution (equation (29)) since we need to solve equation (27) for M(s) and obtain the roots, g_j, then solve for B_j from equation (29). The choice of K is largely dependent on the magnitude of $(F\mu)^2/4D$ in equation (25). From our knowledge of previous works, $(F\mu)^2/4D$ is in the order of 10^{-3} near room temperature. Therefore, K=2 was chosen as a first order approximation. Equation (26) is then reduced to

$$\bar{C}_2(s) \simeq \sqrt{s}\, k_2 C_{01} \cdot (s+k_2)^{-1} \cdot \{s\sqrt{s} + \bar{p}\sqrt{D} \cdot s + k_3\sqrt{s} + p\sqrt{D}(\frac{(F\mu)^2}{8D})\}^{-1}. \quad (32)$$

The roots, g_j and B_j are obtained in the same manner as discussed above.

The time dependence of the concentration $C_2(t)$ can be written in a reduced manner as

$$C_2(t) \simeq \sum_{j=1}^{5} B_j \ \mathcal{F}(g_j\sqrt{t}). \quad (33)$$

The mass spectrometer signal is directly proportional to the desorption rate, and may be expressed as

$$I_{ESD}(t) \simeq \beta k_3 \cdot C_2(t) \quad (34)$$

where β is a proportionality constant.

Model Calculation

A quantitative comparison of this model with the experimental data is difficult, since very little is known about the rate coefficients, k_2 and k_3. We have previously used literature data to estimate the diffusion coefficient of sodium in the glass and determined the magnitude of the electric field induced by the electron beam (Chapter II). Using these values, the rate coefficients, k_2 and k_3, can be evaluated by a best fit to the experimental data.

In general, the rate coefficient is dependent upon the beam current density and energy. For a fixed energy, it is expressed [70] as

$$k = j_p \sigma / e \tag{35}$$

where j_p and e are the beam current density and the electronic charge, respectively, and σ is the conversion or desorption cross sections. The cross section is a function of energy, thus the conversion and desorption rates, k_2 and k_3, are respectively expressed as the conversion cross section, $\sigma_{conv.}$, and the desorption cross section, σ_{ESD}. As previously estimated, the value of D and F were taken as 1×10^{-15} cm^2/sec and 1×10^5 V/cm and the mobility is calculated by the Einstein relation, as discussed in Chapter II. The parameter, p, was equated to the reciprocal of the ESD escape depth and was estimated to be ~ 4×10^7 cm^{-1} since ESD originates only from the surface monolayer [88]. The constants, k_2 and k_3, were adjusted for a best fit to the experimental data and the theoretical desorption rate versus the electron bombardment time was calculated. This is shown in Figure 24, where the calculated curves were normalized to their maximum rates. The calculated curves are compared to experimental data corresponding to a beam current density of 1 mA/cm^2 at various primary electron energies (Figures 18(a), (b), (c) and (d)). The error is attributed to statistical variations, but they are systematic deviations when considering a long period of time. The time required to reach the maximum

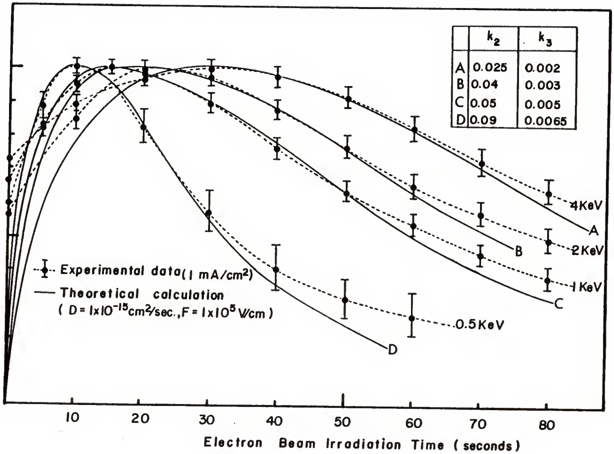

Figure 24. Calculated desorption rates of sodium from the soda-silica glass surface that are best fit to the experimental data reproduced from Figure 20.

desorption rate and the decay rate are well matched by the calculated data. The conversion cross section and the desorption cross section for each energy are evaluated from equation (35) and are summarized in Table 1. The cross sections, $\sigma_{conv.}$ and σ_{ESD}, are on the order of 10^{-18} cm^2 and 10^{-19} cm^2, respectively, and decrease as the energy increases.

Mechanism For Sodium Desorption From Glass Surface

In the previous sections, it has been shown that sodium and oxygen are desorbed from glass surfaces and the kinetics have been modeled in a phenomenological manner. However, the mechanism of sodium desorption is not very obvious. With the conventional Menzel-Gomer-Redhead ESD model [95 , 96] sodium desorption from the soda-silica glass cannot be fully explained. Instead, a mechanism proposed by Knotek and Feibelman [97 ,109], an interatomic Auger de-excitation model, can be applied to the present case.

Knotek and Feibelman [97 ,109] have formulated a mechanism for ESD of positive ions from maximal valence transition metal oxides, i.e., oxides in which the metal cation is ionized to the rare gas configuration (e.g., Ti^{4+} in TiO_2). In the metal oxides with a high negative charge on the oxygen, the production of positive oxygen is only possible by multiple ionization. An interatomic Auger process can cause multiple ionization, starting with the creation of an inner level electron hole on the cation which is filled by an Auger decay involving the oxygen valence electrons. This leads to a loss of two electrons on the oxygen site. An Auger cascade can lead to an even higher positive charge. A schematic illustration

Table 1. Summary of Calculated Results for the Conversion and the Electron Stimulated Desorption Cross Sections

E_0	500 eV	1000 eV	2000 eV	4000 eV
k_2	0.09	0.05	0.04	0.025
k_3	0.0065	0.005	0.003	0.002
$\sigma_{conv.}$	1.4×10^{-17}	8.0×10^{-18}	6.4×10^{-18}	4.0×10^{-18}
σ_{ESD}	1.0×10^{-18}	8.0×10^{-19}	4.8×10^{-19}	3.2×10^{-19}
	Unit of cross section (cm^2)			

of an interatomic Auger decay in TiO_2, for example, is shown in Figure 25. The highest occupied level of the Ti^{4+} is Ti-3p level of ~ 34 eV since there are no electrons in the valence band. If an electron ionizes this level, the dominant decay mode will be an interatomic Auger decay, since the valence electron density on the Ti ion is too low for intra-atomic Auger decay to be a likely process. Therefore, one of the O-2p electrons decays into the Ti-3p hole and another electron is ejected from the O-2p level in the Auger process. The O^{2-} ion is thus converted to an O^0. If one of the remaining valence electrons is shared between the O and Ti (recall that in equilibrium an O is not O^{2-} but $O^{(1+x)-}$) then there is an appreciable probability that O will desorb as O^+.

This picture is now applied to our case. When the freshly created soda-silica glass surface is bombarded by electrons, they will break the O-Na bond and the unsatisfied non-bridging oxygen bond will trap a hole in a non-bonding 2p orbital of oxygen, resulting in a $Si^{4+}O^{1-}Na^{1+}$ configuration. If the sodium desorbs as Na^{1+}, it only occurs via Coulombic repulsion with O^{1+} ions. Therefore, oxygen has to be converted into positive oxygen. This can occur either by intraatomic Auger de-excitation at oxygen or interatomic Auger de-excitation as applied to $Si^{4+}O^{1-}$. An energy diagram for $Si^{4+}O^{1-}Na^{1+}$ is given in Figure 26.

Intraatomic Auger de-excitation. The highest occupied level of O^- is O-2p level, which forms a valence band. From photoemission measurements of the valence level of amorphous SiO_2 [114] the valence band consists of non-bonding and bonding bands. These are considerably broad with band widths of approximately 3.2 eV and 5.7 eV, respectively. When the incident

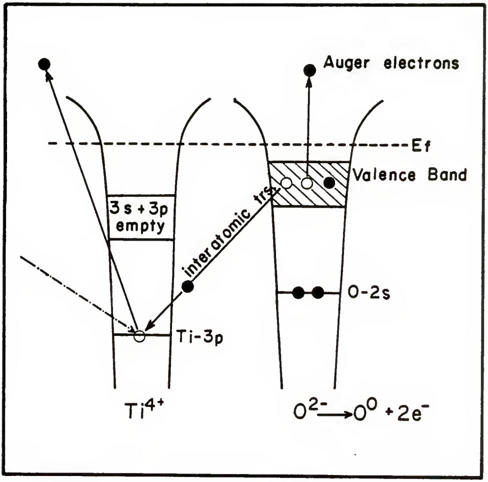

Figure 25. Interatomic Auger de-excitation model for stimulated desorption of ions. Formulation of a core hole in the 3p shell of maximal valency TiO_2 is followed by interatomic Auger decay.

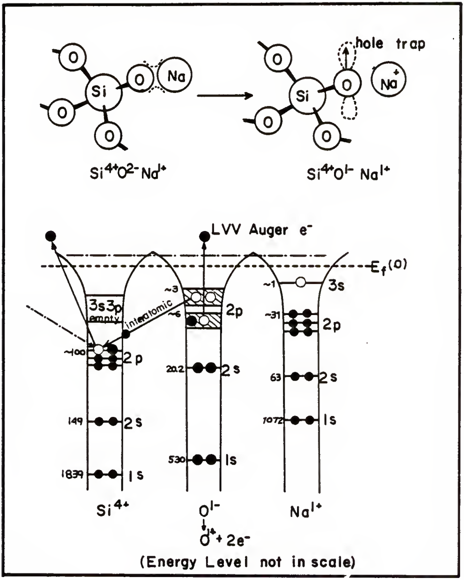

(Energy Level not in scale)

Figure 26. Interatomic Auger de-excitation model for stimulated desorption of sodium ions. After a hole trapping in non-bridging oxygen 2p orbital of a single oxygen, formulation of a core hole in the 2p shell of maximal valency of Si is followed by interatomic Auger decay.

electron ionizes an O-2s level (L_1), an electron from either the bonding or the non-bonding band occupies the O-2s shell hole and the excess energy is released in the de-excitation by emission of another electron from the valence band (O-LVV Auger electron). The oxygen O^- is thus converted to O^+.

Interatomic Auger de-excitation. The core level, Si-2p($L_{2,3}$) of ~ 100 eV is the highest occupied level in Si^{4+} since no electrons are in the valence band. If an incoming electron ionizes this level, one of the electrons in the O^- valence band (e.g., a 2p non-bonding electron) drops to occupy the Si-2p level by interatomic transition. The energy released by this process is approximately ~100 - ~3 = ~97 eV, which is high enough to eject another electron (O-$L_{2,3}^{Si}V^{O}V^{O}$ Auger electron). This multiple ionization process leaves oxygen as O^+.

The positive oxygen created by either intraatomic or interatomic Auger de-excitation processes results in Coulombic repulsion with Na^+. Thus, the sodium desorbs as Na^+. In addition to sodium desorption, oxygen has to be desorbed as O^+ via Coulombic repulsion with Si^{4+}. Desorption of O^+ was experimentally observed, as discussed in the previous section.

This hypothesis is supported by the data on Na^+ desorption rate versus the primary electron beam energy, as shown in Figure 27. The sodium desorption rate above ~ 100 eV increases rapidly. This indicates that the sodium desorbs mainly via the interatomic Auger de-excitation process since the ionization threshold of the Si-2p level (~ 100 eV) coincides with the primary electron beam energy above which the sodium desorption rate increases drastically. Below 100 eV, a small sodium

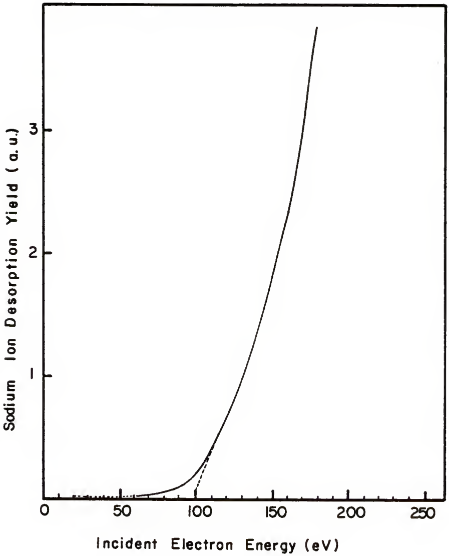

Figure 27. Sodium desorption yield from a soda-silica glass surface versus electron energy.

rate was observed but the signal intensity was weak. Below 60 eV it was too small to be measured. Hence, the threshold energy for intraatomic Auger $L_1^0V^0V^0$ transition, which should be equal to the O-2s ionization energy, 20.2 eV, could not be found experimentally. This data indicates that sodium desorption occurs via an interatomic Auger de-excitation process.

Discussion

As shown in the previous calculation, we have seen a reasonable agreement between the experimental data and the model calculations. A conventional ESD rate equation was not adequate to explain the sodium desorption kinetics, especially the initial rise observed in the sodium desorption rate. An obvious question is whether the initial rise in kinetics is due to surface charging or contamination. For example, the absorption current measured between ground and the specimen during the ESD experiment reached a steady value within a few seconds, while the desorption rate maximum was observed after 10 to 50 seconds, depending on the beam current density. Further bombardment did not vary the absorption current significantly. In addition, the initial rise was much smaller for oxygen desorption rate. In fact, the rate was constant over the period which the sodium desorption rate was increasing. If the initial rise is due to the time-dependent surface charging, the absorption current should have varied [115] and the oxygen desorption rate should have increased, as did the sodium desorption rate. Furthermore, the Auger peak energy did not vary during electron bombardment. This further substantiates that the surface charge was not time-dependent, but only stable charging occurred.

It may also be argued that the initial rise results from surface contamination. As shown in Figure 18, the surface was covered with H_2, F and CO after 90 minutes in a vacuum of 1×10^{-9} Torr. The flux of residual gas molecules which strike the surface per square centimeter per second is proportional to the gas partial pressure [70]. At 1×10^{-9} Torr the flux of gas molecules is about 10^{11} molecules/cm^2 sec. Therefore, after 90 minutes, approximately 5.4×10^{14} molecules of residual gas have collided with one square centimeter of the fracture surface. Since a monolayer is about 10^{15} molecules/cm^2, a 90-minute exposure to 1×10^{-9} Torr will result in less than a monolayer, even if the sticking coefficient is unity for all molecules. The ESD experiment was carried out within 10 to 20 minutes after creation of the surface. Therefore, the contamination on the surface is less than one-tenth of a monolayer for a sticking coefficent of unity. The ESD cross section for adsorbate is about 10^{-16} cm^2 [88]. With such a cross section, 63% of the adsorbates would be desorbed in one second of electron bombardment. Thus, the contamination is not a problem in this case, nor can it be responsible for the initial rise in the sodium desorption rate.

Mechanisms of sodium ESD from glass surfaces were studied and two processes were considered in order to create O^{1+} from O^{1-}. These were intraatomic Auger de-excitation at oxygen and interatomic Auger de-excitation between Si and O. From the threshold measurement, it was found that the interatomic Auger de-excitation was the most likely process. However, there remains a question as to why the intraatomic Auger decay of the oxygen core hole, which also leads to the removal of two valence electrons and thus to the same final state as the Si-2p hole decays, should not lead to a stronger threshold than the interatomic Auger de-excitation process. This can be explained by the law of conservation of energy. In the intraatomic Auger de-excitation process, the maximum energy released by the 2s hole is 20.2 - 3.0 (energy of the valence band maximum) = ~17.2 eV (Figure 26). In order to provide the maximum energy to the desorbing atom (oxygen), we suppose that the second electron in the Auger process is kicked into the conduction band, which has the minimum energy. In the absence of "hole-hole interaction," this energy would be the band gap energy, i.e., ~3 eV above the Fermi energy level [114]. However, it is known that a second electron from the oxygen sitting in the Madelung potential will require more energy than that to remove the first valence electron. This additional energy is just the "hole-hole repulsion" energy. This may be evaluated by a comparison of KVV Auger data with x-ray photoemission results, to be on the order of 6 eV [116]. Thus, the minimum energy required to remove the second valence electron from an O atom is then 6 + 3 + 6 ≃ 15 eV. Therefore, the kinetic energy of the O^+ is only 17.2 - 15 ≃ 2.2 eV. By contrast, much more kinetic energy is available in the interatomic Auger process, since the Si-2p ionization energy is about 100 eV, which is ~ 80 eV higher in the kinetic energy of desorbing O^+ ions. Consequently, the desorption via interatomic Auger de-excitation is the most likely process.

Because of the large charge transfer involved in the ESD process, it may be anticipated that ESD data provides further information bearing on the states and valencies of bonding in the outermost layer of a solid.

This may be extremely useful to study the early stage glass surface reaction with environment (for example, weathering and ion exchange processes). This unique capability of ESD is a consequence of the facts that: (1) a core electron must be excited to initiate desorption, thus, giving rise to a bonding-state-dependent threshold energy, and (2) a nearest neighbor atom is involved in an interatomic Auger de-excitation, which results in valence sensitivity. Thus, ESD can be a probe of the valence of bonding at a surface and it is promised that careful threshold measurement will provide important information directly.

The ESD cross section can be estimated based on the fundamental mechanism. The interatomic Auger process is one in which a primary electron creates a core hole of a parent atom followed by an Auger neutralization from a nearest neighbor atom. Therefore, the sodium ESD cross section is equal to the product of the inner shell ionization cross section of Si-2p and the probability of sodium via Coulombic repulsion is unity. McGuire [117] has calculated the Si-2p ionization cross section based upon the Bethe theory [99]. For primary energies between 0.5 and 4.0 keV, ionization cross sections of ~ 4×10^{-18} to ~ 2×10^{-18} cm^2 were reported. A similar value of cross section was obtained experimentally by Meyer and Vrakking [118,119]. Since the interatomic transition rate is very fast (~ 10^{-14} seconds [120]), the probability of the Auger neutralization is only limited by the density of state of the oxygen valence band. Because of the localized electron states in the oxygen valence band, i.e., non-bonding and bonding electrons, the probability of the Auger neutralization is low [121]. Furthermore, the survival probability for O^+ via Auger neutralization is ~ 0.01 to ~ 0.1 [120]. Thus, the estimated sodium ESD cross section is ~ 10^{-19} cm^2 or less. This is still smaller than the value determined by the experiment (~ 10^{-19} cm^2); however, the calculation provides a lower limit on the possible ESD cross section.

In the ESD threshold measurement, the energy was only scanned up to 200 eV, therefore, only the oxygen $L_{2,3}VV$ transition was possible. If the energy is increased, the oxygen KLL transition would occur. It is speculated that the desorption rate would increase more when the oxygen K edge was crossed at 530 eV. Because of this, the probability for oxygen multiple ionization would increase with higher energy, resulting in a higher sodium desorption. Therefore, the observed sodium ESD cross section of 10^{-19} cm^2 is very reasonable.

In electron stimulated desorption of sodium, the desorption rate increased when the beam current density was increased (Figure 21), but not linearly. Based upon the present model, the dependence of the maximum desorption rate upon current density is evaluated from equation (19) and is shown in Figure 28. For a small beam current density, the desorption rate was negligible, and thus, ESD is not important. As the current density is increase to more than 10^{-3} A/cm^2, the maximum desorption rate increases. The desorption rate does not continue to increase, but tends to saturate at a very high beam current density. This means that ESD becomes important at beam current density > 10^{-3} A/cm^2, but at beam current densities ~ 10^{-2} A/cm^2 diffusion limits further increase in the ESD rate. In a typical AES experiment, a beam current density range of 10^{-4} to 10^{-2} A/cm^2 is used. This is the range where ESD becomes important.

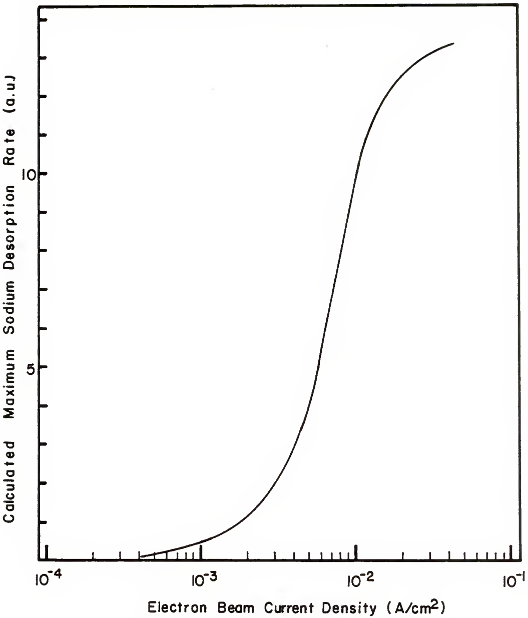

Figure 28. Calculated maximum desorption rate of sodium from the soda-silica glass surface as a function of beam current density.

While the proposed model correctly predicts the rise and the fall in the sodium desorption rate, it predicts that the rate should be zero at $t = 0$ (Figure 24). The initial conditions we have used to obtain the solutions are applied to ideal surface conditions, i.e., no defects at the surface before electron bombardment. However, this may not be true in a real case. Fracturing is essentially a bond break and defects are formed. Therefore, it is probable that non-bonded sodium exists prior to the electron bombardment. In this case, the initial condition (14) should be changed to

$$C_2(0) = C_{02} \qquad (36)$$

where C_{02} is the concentration of non-bonded sodium ions before electron bombardment. However, solving the equation with this initial condition is not easy because a discontinuity now exists at $z = 0$, making it difficult to find the Laplace transform of $C_b(z,t)$. This is one difficulty. In addition, the concentration of non-bonded sodium ions, C_{02}, is difficult to quantify and varies from one experiment to the next. Because of this, a calculation using the appropriate initial conditions was not attempted.

Summary

1. Electron stimulated desorption of sodium from *in situ* fractured soda-silica glass surfaces has been studied. The desorption rate was dependent upon the electron beam energy, current density and bombardment time.

2. The desorption rate of sodium first increased, followed by a monotonic decrease. This initial rise in the rate cannot be explained by a conventional ESD rate equation. It was found that the initial rise in the desorption rate was an inherent characteristic of ESD from glass.
3. A phenomenological model was developed considering processes involving production of ion pair, followed by a hole trap at the oxygen site and electron stimulated desorption and field-enhanced diffusion. The model predicts correctly the kinetics of sodium desorption.
4. The electron stimulated desorption cross section was evaluated to be about 10^{-19} cm^2 by comparing the experimental data with the model. It decreased when the energy was increased.
5. A mechanism for sodium desorption from soda-silica glass was developed by considering intraatomic and interatomic Auger de-excitation processes. For the primary electron energies above 100 eV, the interatomic Auger de-excitation process is the most likely. ESD cross section was estimated based upon the fundamental principle and it was shown that the value of experimentally determined ESD cross sections was very reasonable.
6. Because of the large charge transfer involved in the ESD process, ESD can be a valence-sensitive probe at a surface. Careful threshold measurement may provide important information of a surface directly.
7. ESD is important in a conventional AES analysis when beam current densities $> 10^{-3}$ A/cm^2 are used.

CHAPTER IV
THEORETICAL INTERPRETATION OF ALKALI AUGER SIGNAL DECAY PROCESS

We have shown that the decay of an alkali Auger signal at the glass surface during analysis with Auger electron spectroscopy was a result of its diffusion into the bulk and its desorption from the surface under the influence of the electron beam. The magnitudes of these two effects were dependent upon electron beam energy, beam current density, substrate temperature and amount of contamination on the surface. These parameters have to be carefully controlled for accurate and precise Auger analysis.

The observation of an "incubation time" during AES of the glass surface [39] is interesting. During the incubation time, the alkali concentration can be determined if the AES measurement is accomplished within this period. The length of the incubation time varies strongly with the electron beam conditions, the glass composition and the temperature. These features have been found experimentally. However, neither a comprehensive explanation of the origin of the incubation time nor a theoretical prediction has been made.

In this chapter, we will develop a theory describing the alkali Auger signal decay process. The theory will be applied to low temperature measurements and the origin of the incubation time will become apparent.

Mathematical Formulation of The Alkali Auger Signal Intensity

In Auger electron spectroscopy, the Auger electrons from atoms on the surface and within the outermost atomic layers of the surface can escape without collisions and contribute to the Auger signal. We assume that the Auger intensity is proportional to the concentration of the atoms on the surface and atoms near the surface which have diffused into the bulk. Hence, from the model discussed in Chapter III, the intensity of the alkali Auger signal is

$$I(t)_{\text{Auger}} = \alpha[C_1(t) + C_2(t) + n^A(t)] \tag{37}$$

where α is a proportionality constant and $n^A(t)$ is the number of bulk atoms whose Auger electrons escape from the surface without collision. This latter quantity is expressed as

$$n^A(t) = \int_0^\infty P(z) \cdot C_b(z,t) \cdot dz \tag{38}$$

where P(z) is the probability that the Auger electron will escape. We take [122]

$$P(z) = \exp(-z/\lambda_A) \tag{39}$$

where λ_A is the Auger escape depth (on the order of 10 to 50 Å [66]). Characterization by this simple form is an idealization of the probability which depends on the details of the scattering process, but this approximation has been shown to work well [122]. The concentration of atoms in the bulk is given by equation (15), derived in Chapter IV, thus, $n^A(t)$ is expressed as

$$n^A(t) = \int_0^\infty \int_0^t \exp(-z/\lambda_A) \cdot \frac{pz}{2\sqrt{\pi D}} \cdot \exp(\frac{F\mu}{2D} z - \frac{(F\mu)^2}{4D} \cdot t) \cdot C_2(t')$$

$$X \exp(\frac{(F\mu)^2}{4D} t') \cdot (t-t')^{-3/2} \cdot \exp(- \frac{z^2}{4D}(t-t')^{-1}) dzdt'. \qquad (40)$$

In order to evaluate the integral, we put

$$m = 1/\lambda_A - F\mu/2D \qquad (41)$$

and

$$q = D(t-t') \qquad (42)$$

and we use the fact that [113]

$$\int_0^\infty \exp(-mz) \cdot z \cdot \exp(-z^2/4q)dz = 2q\{-\sqrt{\pi q} \cdot m \cdot e^{qm^2} \cdot \mathrm{erfc}(\sqrt{q}\, m)+1\}. \qquad (43)$$

One can perform the integration over z in equation (40), resulting in

$$n^A(t) = \frac{p}{\sqrt{\pi D}} \cdot h(t) \qquad (44)$$

where

$$h(t) = D \int_0^t \{1-\sqrt{\pi} \cdot y\mathcal{F}(y)\} \cdot C_2(t') \cdot \exp(- \frac{(F\mu)^2}{4D}(t-t')) \cdot (t-t')^{-1/2} dt'. \qquad (45)$$

In equation (45)

$$y = m\sqrt{q} \qquad (46)$$

and

$$\mathcal{F}(y) = e^{y^2} \cdot \mathrm{erf}(y). \qquad (47)$$

We restrict our calculation of the Auger intensities to a small amount of time. When considering only at short times, we can reduce equation (44) to

$$n^A(t) \simeq \frac{p\sqrt{D}}{\sqrt{\pi}} \int_0^t C_2(t')\cdot(t-t')^{-1/2}\cdot\exp(-\frac{(F\mu)^2}{4D}(t-t'))dt'. \qquad (48)$$

Now consider a case where a specimen at liquid nitrogen temperature (110°K) was analyzed. The estimated diffusion coefficient of sodium is about 10^{-30} cm^2/sec and the mobility at this temperature is ~ 10^{-28} cm^2/V sec. Assuming that the electric field is not influenced by the temperature, we take $F = 10^5$ V/cm. With these values, $(F\mu)^2/4D$ is calculated to be ~ 10^{-17} and the exponential term which appeared in equation (48) does not vary at short times. Therefore, we can put

$$\exp(-(F\mu)^2(t-t')/4D) \simeq 1. \qquad (49)$$

Equation (48) can be reduced further to

$$n^A_{\text{low temp.}} \simeq p\sqrt{D}/\sqrt{\pi} \int_0^t C_2(t')\cdot(t-t')^{-1/2}\, dt'. \qquad (50)$$

Recalling the convolution theorem described in Appendix C, we can rewrite equation (50) as

$$n^A_{\text{low temp.}} \simeq p\sqrt{D}/\sqrt{\pi}\cdot \mathcal{L}^{-1}\cdot\{\mathcal{L}(C_2(t))\cdot \mathcal{L}(t^{-1/2})\}. \qquad (51)$$

The Laplace transform of $C_2(t)$ was derived in Chapter III and is equal to

$$\mathcal{L}(C_2(t)) = d\sqrt{s}\cdot(s+k_2)^{-1}\cdot(s\sqrt{s}+as+k_3\sqrt{s}+b)^{-1} \qquad (52)$$

and

$$\mathcal{L}(t^{-1/2}) = \Gamma(1/2)/\sqrt{s} = \sqrt{\pi}/\sqrt{s}. \tag{53}$$

Therefore,

$$\mathcal{L}(C_2(t))\cdot\mathcal{L}(t^{-1/2}) = d\sqrt{\pi}(s+k_2)^{-1}\cdot(s\sqrt{s}+as+k_3\sqrt{s}+b)^{-1}. \tag{54}$$

Using the expansion introduced in Chapter III (equation (14)), equation (54) can be expressed as

$$\mathcal{L}(C_2(t))\cdot\mathcal{L}(t^{-1/2}) \simeq \sqrt{\pi}\sum_{j=1}^{5}\frac{E_j}{\sqrt{s}\cdot(\sqrt{s}+g_j)} \tag{55}$$

where E_j and g_j are constants to be determined.

Substituting equation (55) into equation (51) and taking the inverse Laplace transform, one obtains

$$n^A_{\text{low temp}} \simeq p\sqrt{D}\cdot\sum_{j=1}^{5} E_j\cdot\mathcal{F}(g_j\sqrt{t}). \tag{56}$$

At small t, the function $\mathcal{F}(g_j\sqrt{t})$ can be expanded into a series [113]

$$\mathcal{F}(g_j\sqrt{t}) = 1 - \frac{2}{\sqrt{\pi}}g_j\sqrt{t} + g_j^2\,t + \theta(t). \tag{57}$$

Since $\sum_{j=1}^{5} E_j = 0$, one obtains

$$n^A_{\text{low temp}} \simeq \gamma^A_{1/2}\cdot t^{1/2} + \gamma^A_1\cdot t + \theta^A(t) \tag{58}$$

where

$$\gamma^A_{1/2} = p\sqrt{D}\sum_{j=1}^{5}\left(-\frac{2}{\sqrt{\pi}}E_jg_j\right) \tag{59}$$

and

$$\gamma_1^A = p\sqrt{D} \sum_{j=1}^{5} (E_j g_j^2). \tag{60}$$

The quantity $C_2(t)$ can be expanded in a similar manner when t is small. Thus,

$$C_2(t)_{\text{low temp}} \simeq \gamma_{1/2}^{C_2} \cdot t^{1/2} + \gamma_1^{C_2} \cdot t + \theta^{C_2}(t) \tag{61}$$

where

$$\gamma_{1/2}^{C_2} = \sum_{j=1}^{5} \left(- \frac{2}{\sqrt{\pi}} B_j g_j\right) \tag{62}$$

and

$$\gamma_1^{C_2} = \sum_{j=1}^{5} (B_j g_j^2). \tag{63}$$

Combining equations (58) and (61) with $C_1(t)$, we obtain the alkali Auger intensity expression at low temperature and small t as

$$I(t)^{\text{Auger}}_{\text{low temp}} \simeq \alpha[C_{01}\ e^{-k_2 t} + \gamma_{1/2}^0 t^{1/2} + \gamma_1^0 \cdot t + \theta^0(t)] \tag{64}$$

where

$$\gamma_{1/2}^0 = \gamma_{1/2}^A + \gamma_{1/2}^{C_2} \tag{65}$$

and

$$\gamma_1^0 = \gamma_1^A + \gamma_1^{C_2}. \tag{66}$$

Discussion

A Model Calculation

We have derived the theoretical expression for an alkali Auger signal intensity. Although, the reduced form is only applicable to the case of low temperature measurements for a small t. The time dependence of the intensity can be calculated. A direct comparison of this model with the experimental data is difficult, however, a significant feature observed at low temperatures (the "incubation time") is theoretically predicted.

The sodium Auger intensity from Na_2O-$2SiO_2$ has been calculated using the parameters previously derived from experimental data and literature. The data are:

$D_{Na} = 10^{-30}$ cm^2/sec

$\mu_{Na} = 10^{-28}$ cm/V sec

$F = 10^5$ V/cm

$\sigma_{conv.} = 4.0 \times 10^{-18}$ cm^2 (for 4 keV)

$\sigma_{ESD} = 3.2 \times 10^{-19}$ cm^2 (for 4 keV)

Note that the diffusion coefficient 10^{-30} cm^2/sec corresponds to the constant at 110°K [104].

When a beam current density of 1 mA/cm^2 is chosen for calculation, coefficients appearing in equation (64) are calculated from equations (65) and (66) and the reduced expressions of $C_1(t)$ and $C_2(t) + n^A(t)$ for small t are

$$C_1(t) = C_{01} \exp(-0.025\ t) \qquad (67)$$

and

$$C_2(t) + n^A(t) = C_{01}\ (0.031\ t^{1/2} + 0.010\ t + \theta(t)). \tag{68}$$

The alkali (in this case, sodium) Auger signal intensity is proportional to the sum of equations (67) and (68) as expressed in equation (37). It is obvious that $C_1(t)$ decreases exponentially with time while $C_2(t) + n^A(t)$ increases with time. Calculated curves from equations (67) and (68) are plotted in Figure 29. The quantity $C_2(t) + n^A(t)$ is only plotted up to 15 seconds, since the expression is valid only for a small t. For a large t, we have previously shown that $C_2(t)$ decreases after initial rise (Figure 22). Although the expression for $n^A(t)$ is complicated, it contains $C_2(t)$ explicitly in the integrand, therefore, $n^A(t)$ should decrease, similar to $C_2(t)$ when t becomes large. Thus, $C_2(t) + n^A(t)$ is predicted to be a monotonic decreasing function with time for a large t. However, from equation (68), $C_2(t) + n^A(t)$ increases with time for a small t. The overall expression for the sodium Auger signal intensity is thus a sum of the two curves. This is also shown in Figure 29. The rates of decrease of equation (67) and increase of equation (68) are approximately equal up to ~ 10 seconds. Therefore, the Auger signal intensity does not vary significantly for $t < 10$ seconds (equal to an electron dose of $< 1 \times 10^{-2}$ coulombs/cm^2). This is recognized experimentally and is called an "incubation time." After this initial period of stability, the intensity decays with time. An incubation time is calculated based on the model involving the conversion process, the electron stimulated desorption and the field-enhanced diffusion. The

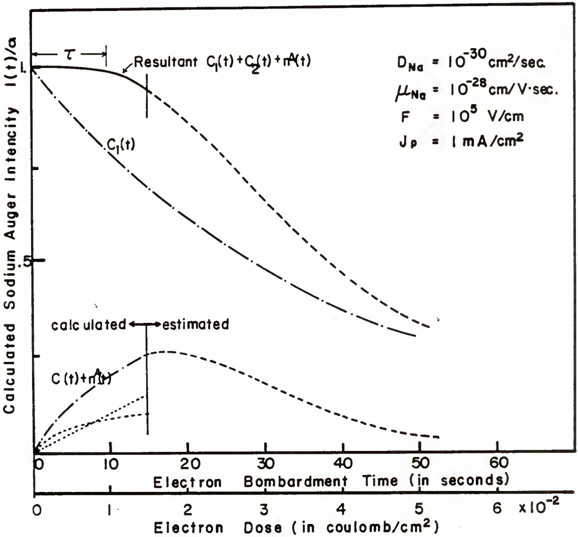

Figure 29. Calculated sodium Auger signal decay from soda-silica glass.

rate of conversion and desorption are controlled primarily by the beam energy and the current density but not by the temperature. The rate of diffusion is strongly dependent upon the temperature. When the temperature is high, the diffusion constant and the mobility are large and diffusion is enhanced. Consequently, the relative magnitudes of $C_2(t)$ become low and $n^A(t)$ decreases correspondingly. This means that the rates of increase in $C_2(t) + n^A(t)$ at room temperature become smaller than those calculated at liquid nitrogen temperature. Therefore, the rate of decrease in $C_1(t)$ is not equivalent to the rate of increase in $C_2(t) + n^A(t)$. The resultant curve, $C_1(t) + C_2(t) + n^A(t)$, shows a monotonic decrease and does not have an initial period at room temperature. The alkali Auger signal only decreases approximately exponentially. This is schematically illustrated in Figure 30.

When the beam current density becomes high at liquid nitrogen temperature, the time response of all the quantities, $C_1(t)$, $C_2(t)$ and $n^A(t)$ becomes shorter since the diffusion is enhanced and it limits increase in ESD rate. Therefore, the rate of initial rise in $C_2(t) + n^A(t)$ may not be as large as the rate of decrease in $C_1(t)$. In this case the incubation time may be shortened or may not be observed. This is consistent with the experimental observation shown in Figure 5 (from [39]). As the beam current density was increased, the incubation time was shortened. At high current density a measurable incubation time was not observed, but the Auger signal decayed approximately exponentially. As expected, at room temperature the incubation time was not observed.

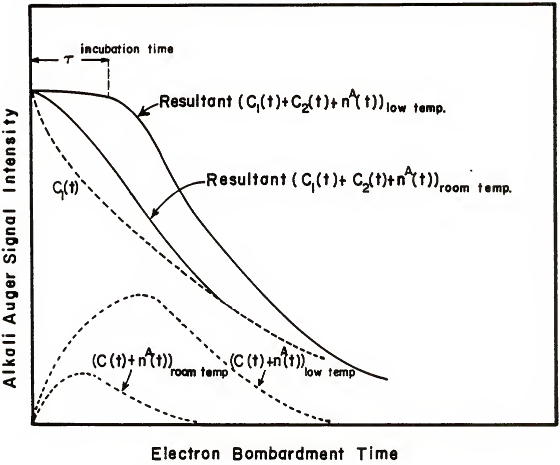

Figure 30. Schematical illustration of relations for $C_1(t)$, $C_2(t)$ and $n^A(t)$ at low temperature and room temperature.

Comparison of Experimental Results with Model

The experimental sodium Auger signal changes from Na_2O-$2SiO_2$ glass are shown in Figure 31, where curves (a) and (b) correspond to the measurements at 110°K and 300°K, respectively. A 3 keV electron beam with 1×10^{-3} A/cm^2 was used for excitation.

No incubation time was observed at room temperature. In this case, the decay curve is divided into three parts (this is clearly seen when the decay curve is plotted on a semi-log scale). In the first decay period (first several seconds), a relatively slow decay rate was observed. Recalling equations (37) and (64), this is a period during which $C_2(t) + n^A(t)$ increases, resulting in a very slow overall decay rate. However, the quantity $C_2(t) + n^A(t)$ decreases subsequently and the decay rate becomes more rapid in the middle part. In the third period there is almost no contribution from $C_2(t) + n^A(t)$, since it asymptotically approaches zero. Thus, the decay in the third period is controlled only by changes in $C_1(t)$. These effects are illustrated in Figure 30.

Upon cooling the sample to 110°K, an incubation time of 15 seconds was observed during which the sodium signal remained unchanged. As shown in the model calculation, the increase in $C_2(t) + n^A(t)$ is balanced by the decrease in $C_1(t)$ in this period. The signal starts to decay subsequently. When the beam current density was changed, the length of incubation time and decay rate varied correspondingly. Plotting the normalized sodium Auger signal versus electron dose (product of beam current density and time) in Figure 32, all the data essentially form a single line. The sodium signals are unchanged up to 1.5×10^{-2} $coulomb/cm^2$. Beyond this

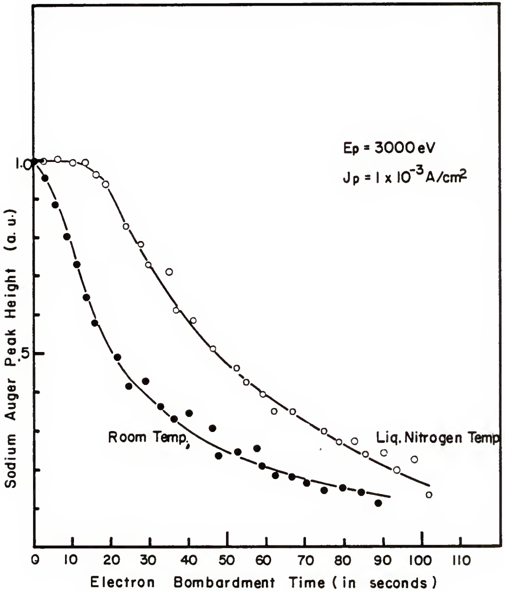

Figure 31. Normalized sodium Auger peak height from soda-disilicate glass as a function of electron beam bombardment time at liquid nitrogen and room temperatures. A 3 keV, 1 mA/cm^2 electron beam was used.

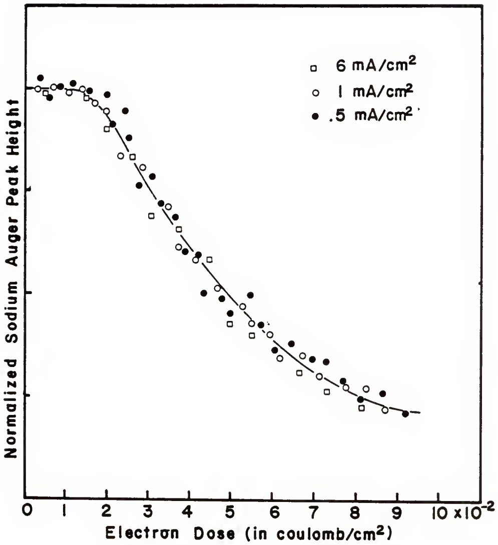

Figure 32. Normalized sodium Auger peak height from a soda-disilicate glass as a function of electron dose at liquid nitrogen temperature (110°K).

doseage, the signal started to decrease. In the model calculation, a similar dosage (~ 1 x 10^{-2} coulomb/cm^2) is calculated for the incubation period. Recently, Pantano and Madey [123] have compiled electron beam damage data reported in the literature. These are reproduced in Table 2. where the critical doses, D_c, are those reported or calculated on the basis of some change in the Auger spectra due to electron beam induced damage. In many of the references, the dose estimates are not precise, so the data are only accurate to an order of magnitude. Nevertheless, it is of interest to note that many organic and inorganic solids exhibit critical doses of 10^{-3} to 10^{-2} coulomb/cm^2. This range of values is consistent with the dose which corresponds to the sodium Auger signal incubation period in Na_2O-$2SiO_2$ glass.

The length of incubation time is very dependent upon the glass composition. We have observed an incubation time of ~ 10 seconds from soda-disilicate glass with beam conditions of 3 keV, 1 mA/cm^2. An incubation time of more than 50 seconds was reported by Pantano [39] (Figure 5) from soda-lime-silica glass under nearly identical experimental conditions. This large difference in incubation time is attributed to the structural differences between the two glasses. In the soda-lime-silica glass, CaO is substituted for SiO_2 of a soda-silica glass. Sodium ions are then bound more tightly in the network [104] and the diffusion constant of sodium is much smaller [104]. Frischart [104] has compared the activation energies for sodium self-diffusion in soda-silica and soda-lime-silica glasses. The values were 20 kcal/mole and 15 kcal/mole in the soda-silica glasses containing Na_2O of 15 and 33 mole %, respectively. Activation

Table 2. Critical Electron Dose for Electron Bombardment Damage of Molecular Solids and Films (from [123])

Material	Energy	D_c(coul/cm^2)	Method	Elements Monitored	Ref.
Si_3N_4	2 keV	stable	AES	O,Si,N	[124]
Al_2O_3	5 keV	10	AES	Al,O	[10]
SiO_2	2 keV	0.6	AES	Si,O	[124]
Li_2WO_4	~1 keV	0.05	XPS	W	[19]
NaF, LiF	.1 keV	0.06	LEED		[14]
$LiNO_3$,$LiSO_4$	1 keV	0.05	XPS,AES	O,S,N	[19]
KCl	1.5 keV	0.03	AES	Cl	[14]
TeO_2	2 keV	0.02	AES	O	[124]
H_2O(F)	1.5 keV	0.01	AES	O	[20]
native oxide	5 keV	0.002	AES		[9]
Na_3AlF_6	3 keV			F	[126]
CH_3OH(F)	1.5 keV	2.5×10^{-4}	AES	C,O	[20]

energies of more than 20 kcal/mole were reported for soda-lime-silica glasses containing equal concentrations of Na_2O. This indicates that the rates of conversion and field-enhanced diffusion of sodium in the soda-lime-silica glass is much slower as compared with the soda-silica glass. The sodium ESD cross section from soda-lime-silica glasses is expected to be similar to one from soda-silica glasses, since the same principle of intraatomic and interatomic Auger de-excitation can be applied. Therefore, the difference in incubation time is due to differences in the rates of conversion and field-enhanced diffusion. Thus, longer incubation times are expected in soda-lime-silica glasses.

Summary

1. A general mathematical description of the alkali signal decay has been developed. It was applied to low temperature measurements and the origin of the incubation time became apparent.
2. Calculations were made of the sodium Auger signal measurements from soda-silica glass at 110°K. It was demonstrated that the sodium Auger signal was nearly constant for an electron dose of $\sim 1 \times 10^{-2}$ coulomb/cm^2 and this was verified by the experiments.
3. Many organic and inorganic solids exhibit electron damage (some change in the Auger spectra due to electron bombardment) within doses of 10^{-3} to 10^{-2} coulomb/cm^2 (from [123]). Therefore, structural interpretation of the surface composition requires careful validation.
4. The length of incubation time varies with the glass composition. Differences in the incubation time are attributed to structural differences;

the higher the bonding strength and the activation energy for alkali diffusion, the longer the incubation time is expected to be.

CHAPTER V
APPLICATION OF ALKALI AUGER SIGNAL DECAY PROCESS FOR MATERIAL CHARACTERIZATION

In the previous chapters, the effects of an electron beam on glass during analysis by Auger electron spectroscopy have been discussed and have been manifested by the alkali Auger signal decay during electron bombardment. Non-recognition of the effects can seriously influence not only quantitative analysis but even qualitative analysis.

However, these effects are sensitive to the composition and structure of the surface and careful interpretation of the effects can provide further information about the surface properties. This will be illustrated in this chapter, where Auger electron spectroscopy will be applied to investigation of microstructural characterization of glass-ceramics.

Glass-ceramics are recognized as extremely important engineering materials with numerous applications [127,128]. These materials are typically prepared from preformed glass castings via a specific nucleation-crystallization treatment. The controlled nucleation-crystallization of glass provides a microstructure of uniform small crystals surrounded by a glassy matrix. The resulting ceramed articles usually have superior mechanical and chemical properties as compared to glass with the same composition [127]. The ceraming process produces local compositional and structural alterations in the materials. These are often difficult to evaluate with conventional x-ray and optical techniques because of the lack of good spatial resolution.

In this chapter, it will be shown that the alkali Auger signal decay process may be used to study the microstructure of glass-ceramics. The rates of alkali Auger signal decay are influenced by the presence of the crystalline phase. The binary Li_2O-$2SiO_2$ system was chosen in the present study because the composition of the crystal is the same as that of the bulk glass for this stoichiometric material.

Experimental Procedure

Lithia-disilicate glass (33 mole % Li_2O and 67 mole % SiO_2) was prepared from reagent grade Li_2CO_3 and 5 μm silica in the manner described earlier in Chapter II. Cast glasses were annealed at 230°C for 4 hours. They were nucleated by heating for 24 hours at 475°C and partially crystallized under the conditions shown in Table 3. The respective volume fractions of crystallization of $Li_2Si_2O_5$ were ~ 30, ~ 50 and more than 70%, as inferred from the data of Freiman and Hench [129]. Scanning electron microscopy† was used to observe fracture surfaces etched with dilute HF. After etching, the specimens were thoroughly rinsed, dried and plated with gold-palladium by vacuum deposition.

The Auger measurements were made in a manner similar to those described in Chapter II. A Physical Electronics Thin Film Analyzer†† was used. All the spectra were obtained with a 1 keV electron beam. The specimens were cooled to ~ 110°K by feeding liquid nitrogen into a carousel. The specimen

---

† Cambridge Stereoscan, Kent Cambridge Scientific, Inc., Morton Grove, IL

†† CMA 10-150, Perkin Elmer, Physical Electronics Division, Eden Prairie, MN

Table 3. Specimen Preparation Data

	Annealing		Nucleation		Crystallization	
	Temp(°C)	Time(h)	Temp(°C)	Time(h)	Temp(°C)	Time(h)
0% glass	230	4	---	--	---	
30% glass-ceramic	230	4	475	24	550	3.3
50% glass-ceramic	230	4	475	24	550	8.3
>70% glass-ceramic	230	4	475	24	550	24

temperature could be varied between 110°K and room temperature by simultaneous cooling with liquid nitrogen and heating with an electric heater installed in the carousel. The temperature was measured with a Chromel-Alumel thermocouple[†] sandwiched between two glass slides and mounted on the carousel.

Results

Scanning electron micrographs of etched fracture surfaces are shown in Figure 33. The formation of rod-like crystals reported by Freiman and Hench [129] is evident. The glass-ceramics containing 50% crystal (b) indicates the crystal growth occurs to impingement. It appears that the residual matrices apparently crystallize in a dendritic fashion. This secondary crystallization apparently produces small crystallite within the interstices of the impinged spherulites [130]. This is no longer evident in the glass ceramics containing more than 70% crystal (a). The glass phase apparently exists in continuous crystal phases.

A plot of the lithium Auger peak height variation as a function of beam bombardment time for the uncrystallized glass is shown in Figure 34. The data were taken at ~ 110°K. As expected, the decay rates were strongly dependent on the beam current densities and faster decay rates were observed with higher beam current densities. Incubation times were observed for beam current densities of $\leq 1 \times 10^{-3}$ A/cm^2. For example, at 7×10^{-4} A/cm^2, the incubation time was about 20 seconds (equal to an electron does of $\sim 1.4 \times 10^{-2}$ coulomb/cm^2).

[†] Hoskins Manufacturing Company, Detroit, MI

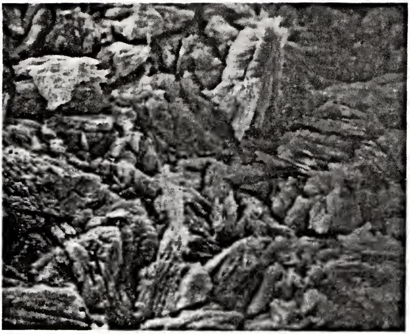

(a) more than 70%

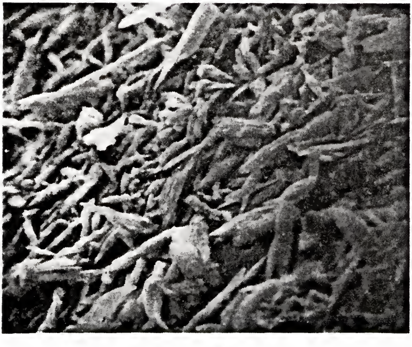

(b) ~50% (mag. x1000)

Figure 33. Scanning electron micrographs of etched fracture surface of lithi-disilicate glass containing: (a) more than 70% crystallization and (b) approximately 50% crystallization.

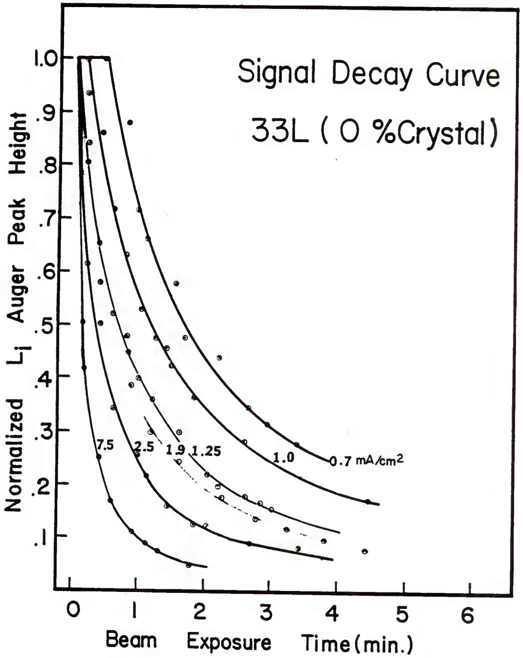

Figure 34. Lithium Auger peak height as a function of beam exposure time and beam current density for lithia-disilicate glass at liquid nitrogen temperature (110°K).

The lithium Auger signal versus irradition time from glass ceramics with 30% (by volume) crystallization is shown in Figure 35. Incubation times similar to the uncrystallized glass were observed. As the beam current density was increased, the decay rate was accelerated as expected, but there were additional features in the decay which were not observed in the uncrystallized glass. Three regions of behavior in the lithium Auger signal decay were observed, as shown in Figure 35. In region I, the signal for the glass-ceramic decayed at approximately the same rate as the glass for identical beam conditions. The rates of signal decays, however, became considerably slower in glass-ceramics for all beam current densities, as indicated in region II. For a current density of 1.25×10^{-3} A/cm^2 the signal was nearly independent of beam irradiation time. In region III, the signal again decayed, but the rate was less than for glass. The extent of each region was strongly dependent upon the beam current density.

Similar results were obtained for the glass-ceramics with higher volume fraction crystallinity. The decay curves for four volume fractions of crystallization (0%, ~30%, ~50% and more than 79% crystalline) are shown in Figure 36. These data were obtained with a current density of 1.25×10^{-3} A/cm^2 at ~ 110°K. For each glass-ceramic specimen, the lithium Auger signal decayed rapidly in region I, followed by a nearly constant signal which was independent of the beam irradiation time (region II). Decay was again observed in region III.

The temperature dependence in the lithium Auger signal decay from the ~30% crystallized specimen is shown in Figure 37. A 1 keV, 1.25×10^{-3}

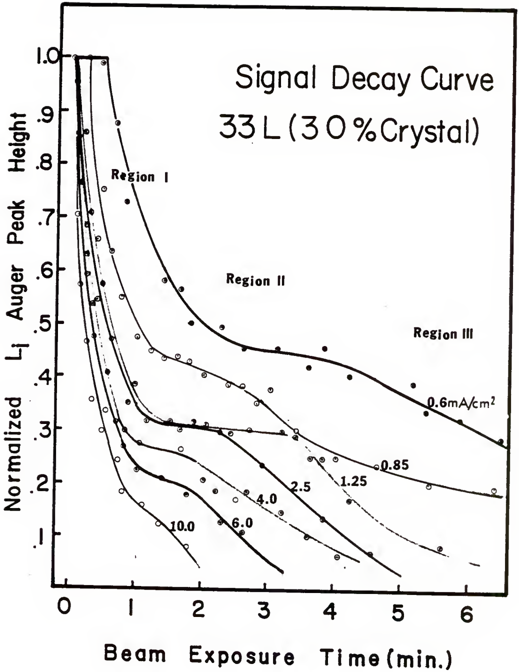

Figure 35. Lithium Auger peak height as a function of beam exposure time and beam current density for lithia-disilicate glass containing 30% crystallization at liquid nitrogen temperature.

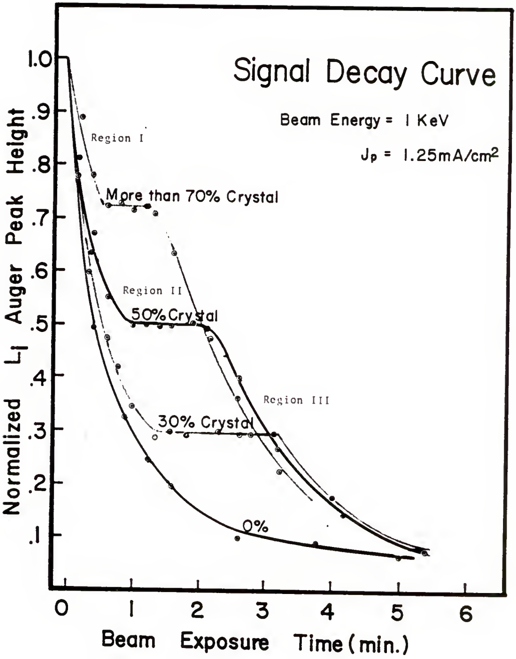

Figure 36. Lithium Auger peak height as a function of beam exposure time for various volume fractions of crystallization.

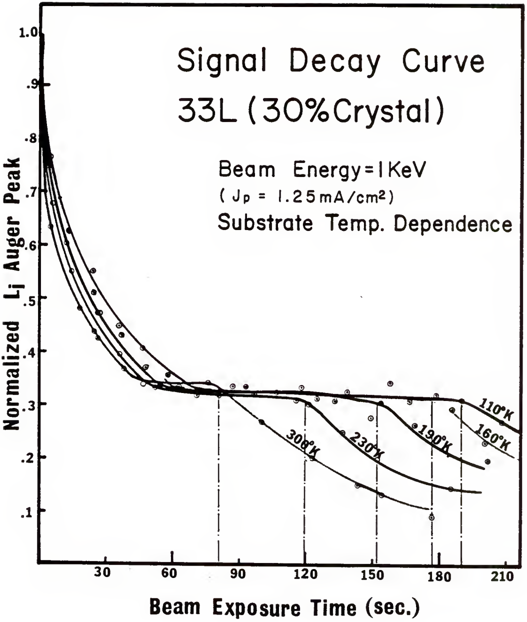

Figure 37. Lithium Auger peak height as a function of substrate temperature for 33L glass containing 30% crystallization.

A/cm^2 electron beam was used. A length of region II progressively decreased as the specimen temperature increased.

Discussion

The lithium Auger signal decays from glass and from glass-ceramics were considerably different. It was shown that the decay rates from glass-ceramics were nearly identical to those from glass during early electron bombardment but became significantly different upon further bombardment. These were clearly shown by comparing the Auger decays from uncrystallized glass (Figure 34) with those from 30% crystallized glass (Figure 35). In both specimens, nearly identical decay rates were observed in the first 60 seconds (region I). These data suggest that the lithium ions in the glass phase of the glass-ceramics are responsible for the Auger signal loss. After the lithium ions in the glass phase were depleted, the Auger signals in region II are due primarily to the lithium ions in the crystal phase. These features are further substantiated in Figure 36, when a beam current density of 1.25×10^{-3} A/cm^2 was chosen. The Auger signal remained relatively constant in region II and its normalized value corresponds to the percent of crystallization. We will define this period as a "ceramic incubation time," similar to an incubation time observed in glass.

The existence of a relatively long "ceramic incubation time" for the crystalline phase is reasonable based upon its properties. For example, (1) the diffusion coefficient of Li in the crystalline phase is at least 10^2 to 10^3 times lower than that in the glass of the same composition [131], (2) the crystalline phase has a higher thermal conductivity than the glass phase of the same composition [131,132] and (3) the bond between the Li ion and the non-bridging oxygen is stronger in the crystalline phase than in the glass phase [131]. From these facts, the ceramic incubation time is interpreted from the discussion described in Chapter IV in a qualitative sense. For the crystalline phase, because of the higher bond strength between Li and O, the rate of $Si^{4+}O^{1-}Li^{1+}$ defect formation, or the conversion rate, k_2, is low. Thus, the exponential decay of $C_1(t)$ in equation (37) is slow. Local heating due to the electron beam is expected to be smaller for the same power input because of the higher thermal conductivity. The field-enhanced diffusion is also smaller because of the lower diffusion coefficient. Therefore, the increase in $C_2(t) + n^A(t)$ is extended to a longer bombardment time and it is balanced with the decrease in $C_1(t)$. Consequently, this results in a longer incubation time in the crystalline phase. This period becomes progressively shorter when the beam current density is increased (Figure 35). In this case, the area being analyzed in the specimen is subjected to higher temperature due to the beam heating and the mobility of Li increases. In addition, the electron stimulated desorption becomes important as the beam current density is increased (in the case of Na, see Figure 26). Therefore, the decrease in ceramic incubation time is attributed to an increase in the rate of diffusion and ESD of Li.

Although the existence of relatively long incubation times was reasonably explained, the ceramic incubation time was shortened as the volume fraction of crystallization increased (Figure 36). This is proposed to result from the power dissipation in the partially crystallized specimens. Although the thermal conductivity in the crystalline phase is higher, an increase in the crystallized volume fraction introduces porosity (due to thermal stress at the phase boundary), as shown in the scanning electron micrographs (Figure 33). Thereby, the overall thermal conductivity of the composite decreases due to increased phonon scattering and a lower conduction heat flux. Therefore, the local temperature from the electron beam would increase as the volume fraction of crystallization increased, with other factors remaining constant. Besides a higher local temperature, the deposited charges (electrons) tend to accumulate at phase boundaries of individual crystallites [115]. The amount of charge accumulation is thereby increased and a higher electric field may result. Higher local temperatures and higher electric fields increase Li mobility and the diffusion driving force, which results in an increased field-enhanced diffusion rate. The ceramic incubation time observed in specimens with a high volume fraction of crystallization is therefore decreased. This hypothesis was tested by looking at the ceramic incubation time as a function of the substrate temperature, as shown in Figure 37. As the temperature of the specimen increased, the local temperature correspondingly increased for a constant beam power. Thus, the lithium mobility increased and the field-enhanced diffusion rate increased correspondingly, resulting in shorter ceramic incubation times at higher temperatures.

The discussion presented above shows that thermal conduction plays an important role in the rate of the alkali Auger signal decay in the composite material. The thermal conductivity is strongly dependent upon the specimen microstructure; therefore, careful interpretation is necessary for Auger analysis of the composite material. Nevertheless, the present study indicates that the electron beam effects can be used to provide a basis for Auger electron spectroscopic studies of microstructural, as well as compositional properties.

Summary

1. Lithium Auger signal variation has been studied from the lithia-disilicate glasses containing $Li_2Si_2O_5$ crystallite with a volume fraction of 0%, ~30%, ~50% and more than 70%.
2. The rates of decay of the lithium Auger signals from crystallized glasses were influenced by the presence of the crystalline phase and were strongly dependent on beam current density.
3. Upon choosing an appropriate beam current density, the decay curve from crystallized glasses was divided into three regions with respect to electron bombardment time. (a) Region I: the decay characteristics were identical to those of uncrystallized glass and were attributed to the lithium Auger signal decay in the glass phase. (b) Region II: the lithium Auger signal remained constant and its normalized intensity corresponded to the percent of crystallization. This period was named "ceramic incubation time." (c) Region III: this lithium Auger signal decay was attributed to the crystalline phase of the material.
4. The ceramic incubation time was interpreted from the general alkali Auger signal decay theory developed in Chapter IV.

5. The ceramic incubation time decreased as the volume fraction of crystallization increased. This was explained by the power dissipation and the charge accumulation in the partially crystallized specimens.
6. The present study indicates that the electron beam effects can be used to provide a basis for Auger electron spectroscopic studies of microstructure as well as composition.

CHAPTER VI
SUMMARY AND CONCLUSIONS

The goal of the present research was to investigate possible mechanisms of alkali Auger signal loss on glass surfaces during electron bombardment. It was concluded that the signal loss was caused by the disappearance of alkali ions at the surface due to electron stimulated desorption and electric field enhanced diffusion. This was modeled by considering the following processes: An energetic electron will break a bond to create an ion pair of oxygen and alkali ions at the surface. The oxygen ion will then trap a hole and the alkali ion will no longer be bound. Further bombardment by electrons will cause an electronic excitation of oxygen (de-excitation) followed by an escape of the alkali ion via coulombic repulsion (electron stimulated desorption). In addition, an electric field is produced normal to the surface as a result of the surface positive potential and the diffused negative layer at a depth equal to the electron range. Under the influence of this electric field the alkali ions diffuse away from the surface (electric field enhanced diffusion). This is further accelerated when electron beam heating causes an increase in temperature, resulting in higher alkali mobility.

This general model was then formulated mathematically and a closed form of analytical solution was found. The solution includes all the experimental parameters, such as electron beam energy, current density, bombardment time and temperature; and the material parameters, such as diffusion constant and mobility. Relative contributions of desorption and diffusion to the processes were calculated and it was found that ESD becomes important with beam current densities greater than 10^{-3} A/cm^2 but the diffusion limited further increase in ESD with densities greater than 5×10^{-2} A/cm^2. In a conventional AES analysis of glass surfaces, both desorption and diffusion are occurring and are important.

An incubation time during which the alkali Auger signal is constant was demonstrated by the general model, when the solution was applied to the case of low temperature. For soda-silica glass, the sodium Auger signal was nearly consistent within a dose of ~ 1×10^{-2} coulomb/cm^2 and this was verified experimentally. In this case, the incubation time was only several seconds when an electron beam with ~ 10^{-3} A/cm^2 range was used. It is emphasized that the analysis has to be made within this time after the electron gun was turned on and the data taken after this time is not meaningful. The reluctance to recognize the effect can seriously influence the analysis. The length of the incubation time is also dependent upon the glass composition. It follows from theory that glasses containing alkali ions with lower diffusion constants and higher bonding strengths result in longer incubation times (for example, soda-lime-silica glass). Thus, the theory developed in the present work has a practical importance for glass surface analysis by AES.

Electric field enhanced diffusion of sodium was demonstrated in soda-silica glass thin films deposited on stainless steel substrates. With these samples, the amount of charge trapping was controlled and the region of the glass over which the diffusion would occur was defined. Thus, a mathematical model was developed and compared with the experimental data. The electron beam raised the temperature of the analysis site by approximately 200°C and the field strength was determined to be approximately 10^5 V/cm. The model was also used to calculate the distribution of sodium with depth in the film, but the calculated distribution disagreed with experimental sputter profile data. This results from redistribution of sodium during Ar^+ bombardment for sputter profiling.

Sodium desorption kinetics were studied from soda-silica glass surfaces fractured *in situ*. It was well explained by the general model described above. The ESD cross section was evaluated to be approximately 10^{-19} cm^2 and decreased as the primary electron energy increased. A conventional ESD mechanism (Menzel-Gomer-Redhead model) was not adequate to explain the sodium desorption from glass. In this case, sodium desorbs via intraatomic Auger de-excitation for the primary electron energies of less than 100 eV, while interatomic Auger de-excitation is the most likely mechanism above 100 eV. For higher energies (e.g., $>$ 530 eV), it is speculated that the sodium desorbs via both intra and interatomic Auger de-excitation processes. The ESD cross section was correlated with these mechanisms and the experimentally determined ESD cross section was shown to be very reasonable. Because of unique characteristics of the ESD mechanism, it is suggested that ESD can be a valence-sensitive probe of surfaces and careful measurements of ESD threshold energy and desorbed ion energy distribution may provide further information about the surface. Further investigation of ESD with this point in mind may prove to be very useful.

Finally, AES was applied to the investigation of microstructural characterization of lithia-silica glass-ceramics. The rates of lithium Auger signal decay were influenced by the presence of the crystalline phase. With proper experimental conditions, the decays from glass and crystalline phases were differentiated and the normalized lithium Auger peak height from the crystalline phase corresponded to the percent of crystallization. This feature indicates a basis for AES studies of microstructural as well as compositional properties of materials.

APPENDIX A
SOLUTION OF EQUATION (3)

Equation (3) will be solved for the boundary conditions defined by equations (6) and (7).

If a solution of equation (3) is assumed to be equal to the product of a function Z of z, only distance, and by a function T of only time, t, one obtains

$$T'/T = (DZ'' - EZ')/Z = \text{constant} = -t \qquad \text{(A-1)}$$

where $E = F_{av} \cdot \mu$ and r is as yet unrestricted. Solutions for T and Z are

$$T = \exp(-rt) \qquad \text{(A-2)}$$

$$Z = \exp(Ez/2D) \cdot (K_1 \sin \omega z + K_2 \cos \omega z) \qquad \text{(A-3)}$$

where

$$\omega = (4rD - E^2)^{1/2}/2D. \qquad \text{(A-4)}$$

Solving equation (A-4) for r in terms of ω, substituting this into (A-2), and taking the product of (A-2) and (A-3), one obtains

$$c(z,t) = \exp\{-(4D^2\omega^2 + E^2)t/4D\} \cdot \exp(Ez/2D) \cdot (K_1 \sin \omega z + K_2 \cos \omega z). \qquad \text{(A-5)}$$

The substitution of (A-3) in the boundary conditions leads to the equations

$$K_1 \omega D - 1/2\, K_2 E \qquad \text{(A-6)}$$

$$K_1(\omega D \cos \omega \ell - 1/2E \sin \omega \ell) - K_2(1/2E \cos \omega \ell + \omega D \sin \omega \ell) = 0. \qquad \text{(A-7)}$$

In order that these homogeneous equations possess solutions K_1 and K_2 other than $K_1 = K_2 = 0$, it is necessary that the determinant of the coefficient vanishes. That is

$$\sin \omega\ell \cdot (\omega^2 D^2 + E^2/4) = 0$$

so that

$$\omega = m\pi/\ell \quad m = 0,1,2... \tag{A-8}$$

or

$$\omega = \pm iE/2D. \tag{A-9}$$

The constant ω has one of the values given by (A-8) or (A-9). The ratio of K_1 to K_2 is given by either equations (A-7) or (A-6). If one chooses,

$$K_1 = K_m E$$

then

$$K_2 = K_m \cdot 2m\pi D/\ell.$$

When ω has the value given by (A-9), r is zero, so that T is unity and the corresponding special solution of equation (3) is

$$c = c_0 \exp(Ez/D).$$

Thus, from (A-5), the solution

$$c = \exp\{-(4D^2m^2\pi^2+E^2\ell^2)t/4D\ell^2\} \cdot \exp(Ez/2D) \cdot \sum_1^\infty K_m[E \sin(m\pi z/\ell) + (2m\pi D/\ell) \cdot \cos(m\pi z/\ell)] + K_0 \exp(Ez/D) \tag{A-10}$$

satisfies equation (3) and conditions (6) and (7), where K_m and K_0 have not yet been determined. For $t = 0$, equation (A-10) gives

$$c_0 \exp(-Ez/2D) = K_0 \exp(Ez/2D) + \sum_1^{\infty} K_m [E \sin(m\pi z/\ell) + (2m\pi D/\ell) \cdot \cos(m\pi z/\ell)] \tag{A-11}$$

and it is necessary to determine the constants K_0 and K_m so that this equation will be satisfied. Let

$$u_m = E \sin \omega_m z + 2D\omega_m \cdot \cos \omega_m z \tag{A-12}$$

and

$$u_0 = \exp(Ez/2D) \tag{A-13}$$

where

$$\omega_m = m\pi/\ell \qquad m \neq 0 \quad \text{and} \quad \omega_0^2 = -E^2/4A^2.$$

The function u_i satisfies the differential equation of

$$u_i'' + \omega_i^2 u_i = 0 \qquad i = 0,1,2\ldots \tag{A-14}$$

and the boundary conditions

$$u_i' = E/2D \cdot u_i \qquad z = 0 \text{ and } \ell.$$

Hence, integrating by parts, we obtain,

$$\int_0^{\ell} (u_i'' u_j - u_j'' u_i) dz = [u_i' u_j - u_j' u_i]_0^{\ell} - \int_0^{\ell} (u_i' u_j' - u_j' u_i') dz = 0.$$

From equation (A-14), it follows that

$$\int_0^\ell (u_i''u_j - u_j''u_i)dz = (\omega_j^2 - \omega_i^2) \int_0^\ell u_i u_j dz.$$

Hence, the integral from 0 to ℓ of the product $u_i u_j$ should vanish when $i \neq j$ and only when $i = j$,

$$\int_0^\ell u_i^2 dz = 1/2(E^2 + 4D^2\omega_i^2),\ i \neq 0. \tag{A-15}$$

Using these features, multiplying both sides of equation (A-11) by u_0, and integrating from 0 to ℓ yields

$$K_0 \int_0^\ell \exp(Ez/D)dz = \int_0^\ell c_0 dz = c_0\ell$$

then

$$K_0 = Ec_0\ell/D\{\exp(E\ell/D)-1\}.$$

Similarly, multiplying both sides of equation (A-11) by u_m when $m \neq 0$ and integrating from 0 to ℓ, one obtains

$$K_m = 16D^2Em\pi\ell^3 \cdot \{4D^2m^2\pi^2+E^2\ell^2\}^{-2} \cdot \{1 \pm \exp(-E\ell/2D)\}$$

with the minus sign for m even, and the plus sign for m odd. Substituting K_0 and K_m into equation (A-10), the final solution of equation (3) with conditions (6) and (7) is obtained.

APPENDIX B
SOLUTION OF EQUATION (12)

In this appendix, equation (12) will be solved. It is possible to reduce equation (12) to an ordinary diffusion equation by means of the following transformations [133],

$$C_b(z,t) = C_b^*(z,t) \cdot \exp\left[\frac{F}{2D} z - \frac{(F\mu)^2}{4D} t\right]. \tag{B-1}$$

The reduced form is then

$$\frac{\partial C_b^*(z,t)}{\partial t} = D \frac{\partial^2 C_b^*(z,t)}{\partial z^2} \tag{B-2}$$

and the boundary conditions are

$$C_b^*(0,t) = p\ C_z(t)\ \exp\left(\frac{(F\mu)^2}{4D}\ t\right)$$

and

$$C_b^*(0,0) = 0 \tag{B-3}$$

Introducing the Laplace transformation

$$\bar{C}_b^*(z,s) = \mathcal{L}\{C_b^*(z,t)\}$$

and

$$\bar{C}_2{}^*(z,s) = \mathcal{L}\{C_2(z,t)\}.$$

Equation (B-2) becomes

$$s\bar{C}_b^* = D \frac{\partial^2 \bar{C}^*}{\partial z^2} .$$

Hence, using the boundary conditions (B-3), one obtains

$$\bar{C}_b^*(z,s) = p\bar{C}_2 \cdot (s - \frac{(F\mu)^2}{4D}) \cdot \exp(-z\sqrt{s/D}) \,. \tag{B-4}$$

The inverse Laplace tranformation of the exponential is

$$\mathcal{L}^{-1} \; \exp(-z\sqrt{s/D}) = \kappa \cdot \exp(- \frac{\kappa^2}{t}) \cdot (\pi t^3)^{-1/2}$$

where

$$\kappa = \frac{z}{2\sqrt{D}} \,.$$

Using the face that

$$\mathcal{L}^{-1} \; \{\bar{C}_2(s - \frac{(F\mu)^2}{4D})\} = C_2(t) \cdot \exp(\frac{(F\mu)^2}{4D} t)$$

and the convolution theorem (Appendix C) for Laplace transformation, one obtains

$$C_b^*(z,t) = p \int_0^t C_2(t') \cdot \exp(\frac{(F\ )^2}{4D} t) \cdot \kappa \cdot \exp(-\kappa^2 (t-t')^{-1}) \; (\pi(t-t')^3)^{-1/2} dt' \,. \tag{B-5}$$

APPENDIX C
CONVOLUTION THEOREM

Theorem [134]

If $e^{-s_0 t} f_1(t)$, $e^{-s_0 t} f_2(t)$ are bounded in $t \geq 0$, then

$$\mathcal{L}\{\int_0^t f_1(t-t') \cdot f_2(t')dt'\} = \phi_1 \cdot \phi_2$$

where

$$\phi_1(s) = \mathcal{L}\{f_1(t)\} \text{ and } \phi_2(s) = \mathcal{L}\{f_2(t)\} .$$

APPENDIX D
ELECTRON BEAM HEATING

In order to estimate the temperature in the film, the heat transport shown in the below is considered.

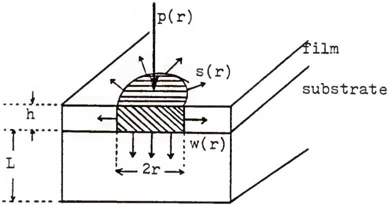

For an arbitrary radius r. the condition of heat balance is

$$\int_0^{r} [p(r')-w(r')]\ 2\pi\ r'dr' - s(r)2\pi rh = 0 \qquad (D\text{-}1)$$

From this, the temperature distribution can be calculated using $w(r) = -\alpha_g(\partial T(r)/\partial Z)$ and $S = -\alpha_m(\partial T(r)/\partial r)$, where α_g and α_m are the thermal conductivities of glass and metal, respectively. Equation (D-1) can be solved approximately for small uniform electron beam (radius to < L). The temperature rise ΔT obtained in the center of the beam is given by

$$\Delta T = pr_o/\alpha_g/(1 + 0.67\ (\alpha_g/\alpha_m)(h/r_o) \qquad (D\text{-}2)$$

Assuming $r_o = 500\ \mu$, $\alpha_m = 2.5\ W\ cm^{-1}\ K^{-1}$, $\alpha_g = 0.01\ W \cdot cm^{-1}\ K^{-1}$ and the input power of $20W\ cm^{-2}$, the temperature is expected to increase approximately 150°C at the film thickness of 3000 Å. At this temperature rise, the sublimation of sodium from glass is negligible.

BIBLIOGRAPHY

1. C. C. Chang, "Analytical Auger Electron Spectrscopy," in Characterization of Solid Surfaces (Plenum, New York, 1974), 509-575.

2. S. H. Hercules and D. M. Hercules, "Surface Characterization by Electron Spectroscopy for Chemical Analysis (ESCA)," in Characterization of Solid Surfaces (Plenum, New York, 1974), 307-335.

3. H. W. Werner, "Introduction to Secondary Ion Mass Spectrometry (SIMS)," in Electron and Ion Spectroscopy of Solids (Plenum, New York, 1978), 324-441.

4. T. M. Buck, "Low-Energy Ion Scattering Spectrometry," in Methods of Surface Analysis (Elsevier Scientific Publishing Co., New York, 1975), 75-100.

5. H. Bach, "Ion Beam-Induced Radiation Applied to Investigations of Thin Surface Layers on Glass Substrates," J. Non-Cryst. Sol., 19, 65-74 (1975).

6. J. F. Ziegler, "Material Analysis by Nuclear Backscattering Introduction," in New Uses of Ion Accelerators (Plenum, New York, 1975), 75-103.

7. C. R. Brundle, "The Application of Electron Spectroscopy to Surface Studies," J. Vac. Sci. Technol., 11(1), 212-24 (1974).

8. S. Thomas, "Electron-Irradiation Effect in the Auger Analysis of SiO_2," J. Appl. Phys., 45(1), 161-6 (1974).

9. J. P. Coad, M. Gettings and J. C. Riviere, "Beam Effects in AES Revealed by XPS," Disc. of Far. Soc., 60, 269-78 (1975).

10. A. Van Oostrom, "Some Aspects of Auger Microanalysis," Surf. Sci., 89, 615-34 (1979).

11. F. Ohuchi, M. Ogino, P. H. Holloway and C. G. Pantano, "Electron Beam Effects During Analysis of Glass Surfaces with Auger Electron Spectroscopy," Surface and Interface Analysis, 2(3), 87-90 (1980).

12. P. W. Palmberg and T. N. Rhodin, "Surface Dissociation of Potassium Chloride by Low Energy Electron Bombardment," J. Phys. Chem. Solids, 29, 1917-24 (1968).

13. R. G. Musket and J. Ferrante, "Auger Electron Spectroscopy Study of Electron Impact Desorption," Surface Sci., 21, 440-2 (1970).

14. H. Tokutaka, M. Prutton, I. G. Higginbotham and T. E. Gallon, "(100) Surface of Alkali Halides II. Electron Stimulated Dissociation," Surf. Sci., 21, 233-40 (1970).

15. C. C. Chang, "Silicon on Sapphire Epitaxy by Vacuum Sublimation — LEED — Auger Studies and Electronic Properties of Films," J. Vac. Sci. Technol., 8, 500-11 (1971).

16. H. H. Madden and G. Ertl, "Decomposition of Carbon Monoxide on a (110) Nickel Surface," Surf. Sci., 35, 211-26 (1973).

17. M. P. Hooker and J. T. Grant, "Auger Electron Spectroscopy Studies of CO on Ni: Spectral Line Shapes and Quantitative Aspects," Surf. Sci., 55, 741-46 (1976).

18. J. C. Fuggle, E. Umbach, P. Feulner and D. Menzel, "Electron Induced Dissociation of CO on RU (001)," Surf. Sci., 64, 69-84 (1977).

19. T. Sasaki, R. S. Williams, J. S. Wong and D. A. Shirley, "Radiation Damage Studies by X-Ray Photoelectron Spectroscopy, I. Electron Irradiated $LiNo_3$ and Li_2SO_4. II. Electron Irradiated Li_2CrO_4 and Li_2WO_4," J. Chem. Phys., 68 and 69, 2718-24 and 4374-80 (1978).

20. P. H. Holloway, T. E. Madey, C. T. Campbell, R. R. Rye and J. E. Houston, "Electron Spectroscopy of Condensed Multilayers: Line Shape Changes Due to Beam Damage and Excitation Mode," Surf. Sci., 88, 121-37 (1979).

21. J. P. Coad, H. E. Bishop and J. C. Riviere, "Electron Beam Assisted Adsorption on the Si (111) Surface," Surf. Sci., 21, 253-64 (1970).

22. J. M. Martinez and J. B. Hudson, "The Adsorption and Decomposition of CO on Pt (111)," J. Vac. Sci. Technol., 10(1), 35-38 (1973).

23. B. A. Joyce and J. H. Neave, "Electron Beam-Adsorbate Interactions on Silicon Surfaces," Surf. Sci., 34, 401-19 (1973).

24. T. N. Taylor and P. J. Estrup, "Carbon Monoxide Adsorption on Ni (110)," J. Vac. Sci. Technol., 10(1), 26-9 (1973).

25. R. E. Kirby and D. Lichtman, "Electron Beam Induced Effects on Gas Adsorption Utilizing Auger Electron Spectroscopy: CO and O_2 on Si, I. Adsorption Studies," Surf. Sci., 41, 447-66 (1974).

26. R. E. Kirby and J. W. Dieball, "Electron Beam Induced Effects on Gas Adsorption Utilizing Auger Electron Spectroscopy: CO and O_2 on Si, II. Structural Effects," Surf. Sci., 41, 467-74 (1974).

27. J. Verhoeven and J. Los, "The Influence of an Electron Beam on Oxidation of Polycrystalline Nickel Surfaces, Monitored by Disappearance Potential Spectroscopy (DAPS)," Surf. Sci., 58, 566-74 (1976).

28. H. G. Tompkins, "The Electron Stimulated Interaction of H_2O with a Nickel Surface," Surf. Sci., 62, 293-297 (1977).

29. R. Riwan, "Diffusion of Sulfur Toward the (110) Face of Nickel," Surf. Sci., 27, 267-72 (1971).

30. J. J. Vrakking and F. Meyer, "Auger Electron Spectroscopy Made Quantitative by Ellipsometric Calibration," Appl. Phys. Lett., 18, 226 (1971).

31. H. Poppa and A. G. Elliott, "The Surface Composition of Mica Substrates," Surf. Sci., 24, 149-63 (1971).

32. C. T. H. Stoddart and E. D. Hondros, "Auger Electron Spectroscopy Study of β''-Alumina Electrolyte," Trans. Brit. Ceram. Soc., 73(2), 61-64 (1974).

33. N. J. Chou, C. M. Osburn, Y. J. van der Meulen and R. Hammer," Auger Analysis of Chlorine in HCl or Cl_2-Grown SiO_2 Films," Appl. Phys. Lett., 22(8), 380-381 (1973).

34. W. C. Johnson and L. A. Heldt, "Composition of Pt Anode Surfaces by Auger Spectroscopy," J. Electrochem. Soc., 121, 34-38 (1974).

35. R. A. Chappell and C. T. H. Stoddart, "An Auger Electron Spectroscopy Study of Float Glass Surfaces," Phys. Chem. Glasses, 15(5), 130-35 (1974).

36. C. G. Pantano, D. B. Dove and G. Y. Onoda, Jr., "AES Analysis of Sodium in a Corroded Bioglass Using a Low-Temperature Technique," Appl. Phys. Lett., 26(11), 601-2 (1975).

37. C. T. H. Stoddart, R. L. Moss and D. Pope, "Determination of the Surface Composition of Palladium-Nickel Alloy Film Catalysts Using Auger Electron Spectroscopy," Surf. Sci., 53, 241-56 (1975).

38. J. Ahn, C. R. Perlebery, D. L. Wilcox, J. W. Coburn and H. F. Winters, "Electron-Beam Effects in Depth Profiling Measurements with Auger Electron Spectroscopy," J. Appl. Phys., 46(10), 4581-4583 (1975).

39. C. G. Pantano, D. B. Dove and G. Y. Onoda, Jr., "AES Compositional Profiles of Mobile Ions in the Surface Region of Glass," J. Vac. Sci. Technol., 13(1), 414-18 (1976).

40. Z. Szklarski-Smialowska, H. Viefhaus and M. Janik-Czachor, "Electron Spectroscopy Analysis of In-Depth Profiles of Iron in Cl-Containing Solutions," Corros. Sci., 16, 649-652 (1976).

41. W. P. Ellis, "Electron-Beam Decomposition of UF_4 Optical Interference Layers," J. Vac. Sci. Technol., 14(6), 1316-7 (1977).

42. H. J. Mathieu, J. B. Mathieu, D. E. McClure and D. Landolt, "Beam Effects in Auger Electron Spectroscopy Analysis of Titanium Oxide Films," J. Vac. Sci. Technol., 14(4), 1023-28 (1977).

43. T. E. Madey, C. D. Wagner and A. Joshi, "Surface Characterization of Catalyts Using Electron Spectroscopies: Results of a Round-Robin Sponsored by ASTM Committee D-32 on Catalysts," J. Electron. Spectrosc. and Rel. Phenom., 10, 359-363 (1977).

44. P. T. Dawson, O. S. Heavens and A. M. Pollard, "Glass Surface Analysis by Auger Electron Spectroscopy," J. Phys. C: Sol. Stat. Phys., 11, 2183-93 (1978).

45. F. Ohuchi, D. E. Clark and L. L. Hench, "Effect of Crystallization on the Auger Electron Signal Decay in a Li_2O-$2SiO_2$ Glass and Glass-Ceramic," J. Am. Cer. Soc., 62, 500-03 (1979).

46. C. G. Pantano and T. N. Wittberg, "Surface Studies of the Medicus Nickel Matrix Cathode," Appl. Surf. Sci., 4, 385-400 (1980).

47. G. T. Burnstein, "Effects of Electron Bombardment During Auger Electron Analysis of Corroded Metal Surfaces," Mat. Sci. and Engr., 42, 207-14 (1980).

48. C. G. Pantano, D. B. Dove and G. Y. Onoda, Jr., "Glass Surface Analysis by Auger Electron Spectroscopy," J. Non-Cryst. Sol., 19, 41-53 (1975).

49. B. J. Todd, "Outgassing of Glass," J. Appl. Phys., 26, 1238-1243 (1955).

50. B. J. Todd, J. L. Lineweaver and J. T. Kerr, "Outgassing Caused by Electron Bombardment of Glass," J. Appl. Phys., 31(1), 51-55 (1960).

51. J. L. Lineweaver, "Oxygen Outgassing Caused by Electron Bombardment of Glass," J. Appl. Phys., 34(6), 1786-1791 (1963).

52. S. Tanaka and D. W. Warrington, "Some Electron Microscope Observations of Thin Film Foils," Phys. Chem. Glasses, 5(3), 87-89 (1964).

53. R. V. Adams, H. Rawson, D. G. Fisher and P. Worthington, "The Use of the Electron Probe X-Ray Microanalyzer for the Identification of Inhomogeneity in Glass," Glass Tech., 7(3), 98-105 (1966).

54. A.K. Varshneya, A. R. Cooper and M. Cable, "Changes in Composition During Electron Microprobe Analysis of K_2O-SrO-SiO_2 Glass," J. Appl. Phys., 37(5), 2199 (1966).

55. M. P. Borom and R. E. Hanneman, "Local Compositional Changes in Alkali Silicate Glasses During Electron Microprobe Analysis," J. Appl. Phys., 38(5), 2406-7 (1967).

56. A. R. Cooper and A. K. Varshneya, "Diffusion in the System K_2O-SrO-SiO_2: I. Effective Binary Diffusion Coefficient," J. Amer. Ceram. Soc., 51(2), 103-106 (1968).

57. L. F. Vassamillet and V. F. Caldwell, "Electron Probe Microanalysis of Alkali Metals in Glasses," J. Appl. Phys., 40(4), 1637-1643 (1969).

58. R. Hayami and H. Wakabayashi, "Changes During Electron Microprobe Analysis of Alkali Silicate Glasses," Yogyo-Kyokai-Shi, 78(896), 138-147 (1970).

59. P. J. Goodhew and J. E. C. Gulley, "Determination of Alkali Metals in Glasses by Electron Probe Microanalysis," Glass Technol., 15(5), 123-126 (1974).

60. D. E. Clark, L. L. Hench and W. A. Acree, "Electron Microprobe Analysis of Na_2O-CaO-SiO_2 Glass," J. Amer. Ceram. Soc., 58(11-12), 531-532 (1975).

61. D. E. Clark, W. A. Acree and L. L. Hench, "Electron Microprobe Analysis of Corroded Soda-Lime-Silica Glasses," J. Amer. Ceram. Soc., 59(9-10), 463-465 (1976).

62. B. Goldstein and D. E. Carlson, "Determination of the Composition of Glass Surfaces by Auger Spectroscopy," J. Amer. Ceram. Soc., 55(1), 51-52 (1972).

63. J. P. Rynd and A. K. Rastogi, "Auger Electron Spectroscopy—A New Tool in the Characterization of Glass Fiber Surfaces," Amer. Ceram. Soc. Bull., 53(9), 631-634, 637 (1974).

64. J. P. Rynd and A. K. Rastogi, "Characterization of Glass Surfaces By Electron Spectroscopy," Surf. Sci., 48(1), 22-43 (1975).

65. C. G. Pantano, Jr., A. E. Clark, Jr. and L. L. Hench, "Multilayer Corrosion Films on Bioglass Surfaces," J. Amer. Ceram. Soc., 57(9), 412-413 (1974).

66. M. P. Seah and W. A. Dench, "Quantitative Electron Spectroscopy of Surfaces: A Standard Data Base for Electron Inelastic Mean Free Paths in Solids," Surface and Interface Anal., 1(1), 2-10 (1979).

67. W. Renter, "Electron Probe Microanalysis," Surf. Sci., 25, 80-119 (1971).

68. M. Tomozawa and R. H. Doremus, Treatise on Materials Science and Technology, Vol. 17, Glass III (Academic Press, New York, 1979).

69. J. Wong and C. A. Angell, Glass Structure by Spectroscopy (Marcel Dekker, Inc., New York, 1976).

70. P. A. Redhead, J. P. Hobson and E. V. Kornelson, The Physical Basis of Ultra-High Vacuum (Chapman and Hall, London, 1968).

71. D. M. Sanders, W. B. Person and L. L. Hench, "Quantitative Analysis of Glass Structure with the Use of Infrared Relfection Spectroscopy," Appl. Spectro., 28(3), 247-255 (1974).

72. L. L. Hench and D. E. Clark, "Physical Chemistry of Glass Surfaces," J. Non-Cryst. Sol., 28, 83-105 (1978).

73. Conventional scanning AES, electron beam spot of ~ 3 μ. PHI 595 Micro Auger Electron Spectroscopy, electron beam spot of 500 Å is obtained from LaB_6 electron source.

74. B. Lang and S. Goldsztaub, "Changing of Insulators in LEED Studies," Surf. Sci., 32, 473-47 (1972).

75. C. H. DeTourreil and K. D. Srivastava, "Mechanism of Surface Charging of High-Voltage Insulators in Vacuum," IEE Trans. on Electrical Insulators," EI-8(1), 17-21 (1973).

76. K. Kanaya, S. Ono and F. Ishigaki, "Secondary Electron Emission From Insulators," J. Phys. D.: Appl. Phys., 11, 2425-2437 (1978).

77. A. P. Janssen, R. C. Shoonmaker, A. Chambers and M. Prutton, "Low Energy Auger and Loss Electron Spectra from Magnesium and Its Oxide," Surf. Sci., 45, 45-60 (1974).

78. C. G. Pantano, Jr., "Compositional Analysis of Glass Surfaces and Their Reaction in Aqueous Environments," Ph.D. Dissertation, University of Florida, Gainesville, FL (1976).

79. B. Carrieré and B. Lang, "A Study of the Charging and Dissociation of SiO_2 Surfaces by AES," Surf. Sci., 64, 209-223 (1977).

80. R. H. Doremus, Glass Science (John Wiley and Sons, New York, 1973).

81. R. G. Gossink and T. P. A. Lommen, "Secondary Ion Mass Spectrometry (SIMS) Analysis of Electron-Bombarded Soda-Lime-Silica Glass," Appl. Phys. Lett., 34(7), 444-446 (1979).

82. M. Watanabe, T. Someya and Y. Nagahama, "Temperature Rise of Specimen Due to Electron Irradiation," J. Phys., D3, 1461-1468 (1970).

83. D. D. Thornburg and C. M. Wayman, "Specimen Temperature Increase During Transmission Electron Microscopy," Phys. Stat. Sol. A, 15, 449-553 (1973).

84. J. M. Short, R. C. Fernquist and W. C. Nixon, "Dynamic Studies of Electron Beam Heating in SEM," Scanning Electron Microscopy (Part I), 45-52 (1976).

85. K. Röll, W. Losch and C. Achete, "Electron Beam-Induced Diffusion During Thin Film Depth Profile," J. Appl. Phys., 50(6), 4422-4424 (1979).

86. Y. Talmon and E. L. Thomas, "Temperature Rise and Sublimation of Water from Thin Frozen Hydrated Specimens in Cold Stage Microscopy," Scanning Electron Micrscopy (Part I), 265-272 (1977).

87. A. W. Mullendore, G. C. Nelson and P. H. Holloway, "Surface Sensitive Analytical Technique: An Evaluation," Proc. Advanc. Tech. Failure Anal., 236-245 (1977).

88. D. Menzel, "Desorption Methods," in Topics in Applied Physics, Vol. 4 (R. Gomer, ed., Springer-Verlag, Berlin, 1975).

89. T. E. Madey and J. T. Yates, Jr., "Electron Stimulated Desorption as a Tool for Studies of Chemisorption: A Review," J. Vac. Sci. Technol., 8, 525-555 (1971).

90. T. E. Madey and Y. T. Yates, Jr., "Desorption Methods as Probes of Kinetics and Bonding at Surfaces," Surf. Sci., 63, 203-31 (1977).

91. J. L. Hock, J. H. Craig, Jr. and D. Lichtman, "Electron Stimulated Desorption of O^+ and O^- From Oxygen Chemisorbed on Tungsten," Surf. Sci., 85, 101-106 (1979).

92. M. L. Knotek, "Characterization of Hydrogen Species on TiO_2 by Electron Stimulated Desorption," Surf. Sci., 91, L17-L22 (1980).

93. R. P. Holmstrom, J. Lagowski and H. C. Gatos, "Electron Beam-Induced Decomposition and Desorption: ZnO," Surf. Sci., 75, L781-L785 (1978).

94. T. T. Lin and D. Lichtman, "The Effects of Electron Bombardment on the Surface Composition of WO_3, Oxidized W and Ta Foils," J. Appl. Phys., 50(3), 1298-1303 (1979).

95. D. Menzel and R. Gomer, "Desorption From Metal Surfaces by Low-Energy Electrons," J. Chem. Phys., 41, 3311-3328 (1964).

96. P. A. Redhead, "Interaction of Slow Electrons with Chemisorbed Oxygen," Can. J. Phys., 42, 886-905 (1964).

97. M. L. Knotek and P. J. Feibelman, "Ion Desorption by Core Hole Auger Decay," Phys. Rev. Lett., 40, 964-967 (1978).

98. H. L. Hughes, "Radiation-Induced Perturbation of the Electrical Properties of Silicon-Silicon/Oxide Interface," IEEE Trans. Nucl. Sci., NS-16(6), 195-202 (1969).

99. H. Bethe, Ann. Phys., 5, 325 (1930).

100. V. E. Cosslett and R. N. Thomas, in The Electron Microprobe (T. D. McKinley, K. F. J. Heinrich and D. B. Wittry, eds., Wiley, New York, 1966) 248.

101. J. I. Goldstein and H. Yokowitz, Practical Scanning Electron Microscopy (Plenum Press, New York, 1975).

102. P. G. Shewmon, Diffusion of Solids (McGraw Hill, New York, 1963).

103. C. G. Pantano, Jr., private communication (Appendix D).

104. G. H. Frischart, Ionic Diffusion in Oxide Glasses (Trans. Tech. Publications, Bay Village, OH, 1975).

105. N. C. MacDonald and T. E. Everhart, "Selective Electron Beam Irradiation of Metal-Oxide-Semiconductor Structure," J. Appl. Phys., 30(5), 2433-2447 (1968).

106. G. W. Morey, The Properties of Glass (Reinhold, New York, 2nd Edition, 1954).

107. D. V. McCaughan, R. A. Kushner and V. T. Murphy, "Ion Neutralization Process at Insulator Surfaces and Consequent Impurity Migration Effects in SiO_2 Films," Phys. Rev. Lett., 30(13), 614-617 (1973).

108. H. D. Hagstrum, "Theory of Auger Neutralization of Ions at the Surface of a Diamond-Type Semiconductor," Phys. Rev., 122(1), 83-113 (1961).

109. P. J. Feibelman and M. L. Knotek, "Reinterpretation of Electron Stimulated Desorption Data from Chemisorption System," Phys. Rev. B, 18(12), 6531-6539 (1978).

110. D. S. Billington and J. H. Crawford, Jr., Radiation Damage in Solids (Princeton University Press, Princeton, NJ, 1961).

111. L. W. Hobbs, Surface and Defect Properties of Solids (The Chemical Society, London, 1975).

112. M. W. Roberts and J. M. Thomas, Surface and Defect Properties of Solids, Vol. 4 (Chemical Society, London, 1975).

113. M. Abramowitz and I. A. Stegun (eds.), Handbook of Mathematical Functions (National Bureau of Standards, Washington, DC, 1964).

114. T. H. DiStefano and D. E. Eastman, "Photoemission Measurement of the Valence Levels of Amorphous SiO_2," Phys. Rev. Lett., 27(23), 1560-1562 (1971).

115. D. A. Moncriett, V. N. E. Robinson and L. B. Harris, "Charge Neutralization of Insulating Surfaces in the SEM Gas Ionization," J. Phys. D: Appl. Phys., 11, 2315-2325 (1978).

116. D. W. Fischer, "X-Ray Band Spectra and Molecular Orbital Structure of Rutile TiO_2m: Phys. Rev. B, 5, 4219-4226 (1972).

117. E. J. McGuire, "Inelastic Scattering of Electrons and Protons by the Elements He to Na," Phys. Rev., A3, 267-279 (1971).

118. F. Meyer and J. J. Vrakking, "Measurement of the Ionization Cross Section of the L_{23}-Shell of Chlorine Using Auger Electron Spectroscopy," Phys. Lett., 44A, 511-512 (1973).

119. J. J. Vrakking and F. Meyer, "Measurement of Ionization Cross Sections and Backscattering Factors of Use in Quantitative AES," Surf. Sci., 47, 50-56 (1975).

120. H. D. Hagstrum, "Studies of Adsorbate Electronic Structure Using Ion Neutralization and Photoemission Spectroscopies," in Electron and Ion Spectroscopy of Solids (Plenum Press, New York, 1978), 273-323.

121. M. Saleron, A. M. Baro and J. M. Rojo, "Interatomic Auger Process and the Density of State," Surf. Sci., 53, 689 (1975).

122. L. A. Harris, "Angular Dependencies of Electron Excited Auger Emission," Surf. Sci., 15, 77-93 (1969).

123. C. G. Pantano, Jr. and T. E. Madey, "Electron Beam Damage in Auger Electron Spectroscopy," to be published in Appl. of Surf. Sci. (1981).

124. Y. E. Strausser and J. S. Johannessen, "An Auger Electron Spectroscopy Study of Silicon Spectra from Silicon Monoxide, Silicon Dioxide and Silicon Nitride," in Surface Analysis for Silicon Devices (NBS Special Publ. 400-23, Washington, DC, 1977), 125.

125. R. G. Musket, "Studies of Clean and Oxidized Tellurium Surfaces," Surf. Sci., 74, 423-36 (1978).

126. In the Proceedings of the 7th Intl. Vac. Congr. and 3rd Intl. Conf. on Solid Surf. (Vienna, Austria, 1977).

127. A. G. Pincus, "Application of Glass-Ceramics," in Advances in Nucleation and Crystallization in Glasses (The American Ceramic Society, Columbus, OH, 1971), 210-223.

128. G. H. Beall, "Structure, Properties and Application of Glass-Ceramics," in Advances in Nucleation and Crystallization in Glasses (The American Ceramic Society, Columbus, OH, 1971), 251-261.

129. S. W. Freiman and L. L. Hench, "Kinetics of Crystallization in Li_2O-SiO_2 Glasses," J. Amer. Ceram. Soc., 51(7), 382-387 (1968).

130. S. W. Freiman, G. Y. Onoda, Jr. and A. G. Pincus, "Spherulitic Crystallization in Glasses," in Advances in Nucleation and Crystallization in Glasses (The American Ceramic Society, Columbus, OH, 1971), 141-150.

131. G. H. Frischat, "Comparison of Atom Mobility in Crystalline and Glassy Oxides," in Mass Transport Phenomena in Ceramics (Plenum, New York, 1975), 285-295.

132. W. D. Kingery, H. K. Bowen and D. R. Uhlmann, Introduction to Ceramics (Wiley and Sons, New York, 1976).

133. A. R. Rurth, Handbuck Physik Techn. Mechanik, Vol. 7 (Leipzig, 1931), 635.

134. N. W. McLachlan, Modern Operational Calculus with Applications in Technical Mathematics (MacMillan and Co., Ltd., London, 1948).

BIOGRAPHICAL SKETCH

Fumio Ohuchi was born in Tokyo, Japan, on December 15, 1948. He is the son of Kazuo and Teiko Ohuchi. In March, 1972 he received his B.S. in physics from the Sophia University, Toyko. He continued his graduate work at the Sophia University and graduated in March, 1974, with the degree of Master of Science in physics. He worked as a senior research scientist for O'Hara Optical Glass Manufacturing Company, Kanagawa, Japan from April, 1974 to August, 1975. In September, 1975 he joined the University of Florida as part of the research staff in the Department of Materials Science and Engineering. He started to work on Auger Electron Spectroscopy at this time. In September, 1977, he enrolled in the Graduate School of the University of Florida and is now completing the requirements for the degree of Doctor of Philosophy in materials science and engineering.

His work at the University of Florida has included the design and construction of Auger Electron Spectroscopy and Secondary Ion Mass Spectroscopy; hence a strong familiarity exists with high-vacuum equipment, electron energy analyzer, electron and ion guns, mass spectrometry and related electronics. Research concerned with surface science includes surface physics and chemistry of amorphous and crystal solids. He also has a strong background in surface analytical techniques, including ESCA, ISS, RBS, SEM and EDXA, as well as AES and SIMS.

He has published papers in research areas concerning Auger electron spectroscopy, glass surface reactions and silicon-nitride ceramics. He is a member of the American Vacuum Society, American Ceramic Society, Physical Society of Japan, Keramos Ceramic Engineering honorary, Tau Beta Pi honorary and Alpha Sigma Mu honorary.

Fumio Ohuchi was married to the former Sumiyo Chiba in December, 1976, and has a daughter, Monica, born here in Gainesville, Florida, on January 13, 1981.

I certify that I have read this study and that in my opinion it conforms to acceptable standards of scholarly presentation and is fully adequate, in scope and quality, as a dissertation for the degree of Doctor of Philosophy.

Paul H Holloway

Paul H. Holloway
Associate Professor of Materials
Science and Engineering

I certify that I have read this study and that in my opinion it conforms to acceptable standards of scholarly presentation and is fully adequate, in scope and quality, as a dissertation for the degree of Doctor of Philosophy.

John J. Hren
Professor of Materials Science
and Engineering

I certify that I have read this study and that in my opinion it conforms to acceptable standards of scholarly presentation and is fully adequate, in scope and quality, as a dissertation for the degree of Doctor of Philosophy.

George Y Onoda Jr

George Y. Onoda, Jr.
Professor of Materials Science
and Engineering

I certify that I have read this study and that in my opinion it conforms to acceptable standards of scholarly presentation and is fully adequate, in scope and quality, as a dissertation for the degree of Doctor of Philosophy.

Robert W. Gould
Professor of Materials Science
and Engineering

I certify that I have read this study and that in my opinion it conforms to acceptable standards of scholarly presentation and is fully adequate, in scope and quality, as a dissertation for the degree of Doctor of Philosophy.

Gar B. Hoflund

Gar B. Hoflund
Assistant Professor of Chemical
Engineering

This dissertation was submitted to the Graduate Faculty of the College of Engineering and to the Graduate Council, and was accepted as partial fulfillment of the requirements for the degree of Doctor of Philosophy.

March, 1981

Hubert A. Bevis

Dean, College of Engineering

Dean for Graduate Studies and
Research